

CANCER

IDH3 α regulates one-carbon metabolism in glioblastoma

Jasmine L. May^{1,2}, Fotini M. Kouri^{1,2}, Lisa A. Hurley^{1,2}, Juan Liu³, Serena Tommasini-Ghelfi^{1,2}, Yanrong Ji⁴, Peng Gao⁵, Andrea E. Calvert^{1,2}, Andrew Lee⁶, Navdeep S. Chandel⁷, Ramana V. Davuluri⁴, Craig M. Horbinski^{8,9}, Jason W. Locasale³, Alexander H. Stegh^{1,2*}

Mutation or transcriptional up-regulation of isocitrate dehydrogenases 1 and 2 (*IDH1* and *IDH2*) promotes cancer progression through metabolic reprogramming and epigenetic deregulation of gene expression. Here, we demonstrate that IDH3 α , a subunit of the IDH3 heterotetramer, is elevated in glioblastoma (GBM) patient samples compared to normal brain tissue and promotes GBM progression in orthotopic glioma mouse models. IDH3 α loss of function reduces tricarboxylic acid (TCA) cycle turnover and inhibits oxidative phosphorylation. In addition to its impact on mitochondrial energy metabolism, IDH3 α binds to cytosolic serine hydroxymethyltransferase (cSHMT). This interaction enhances nucleotide availability during DNA replication, while the absence of IDH3 α promotes methionine cycle activity, S-adenosyl methionine generation, and DNA methylation. Thus, the regulation of one-carbon metabolism via an IDH3 α -cSHMT signaling axis represents a novel mechanism of metabolic adaptation in GBM.

INTRODUCTION

Isocitrate dehydrogenases (IDHs) are a group of enzymes that catalyze the oxidative decarboxylation of isocitrate (ICT) to α -ketoglutarate (α KG). Three different IDH paralogs have been identified within eukaryotic cells (1), which localize to different subcellular compartments, use different cofactors, and show different holoenzyme organization and enzymatic characteristics. IDH1 and IDH2 are homodimeric nicotinamide adenine dinucleotide phosphate (NADP⁺)-dependent enzymes that reversibly convert ICT to α KG. In contrast, IDH3 is a nicotinamide adenine dinucleotide (NAD⁺)-dependent heterotetrameric enzyme that irreversibly catalyzes the conversion of ICT to α KG. IDH1 performs its function in the cytosol and peroxisomes, while IDH2 and IDH3 function as part of the tricarboxylic acid (TCA) cycle in the mitochondria.

Oncogenic mutations in *IDH1* and *IDH2* have been identified in acute myelogenous leukemia, low-grade glioma, and secondary glioblastoma (GBM) but are rare in primary or de novo GBM, which represents the vast majority of GBM cases. Point mutations affect the structural organization of the active center and increase the enzymes' affinities for NADPH (reduced form of NADP⁺). Consequently, point-mutated IDH1 and IDH2 catalyze a partial reverse reaction, where α KG is reduced to 2-hydroxyglutarate (2-HG) (2). 2-HG inhibits α KG-dependent dioxygenase function, including

Jumonji C domain-containing histone lysine residue demethylases, resulting in a global hypermethylation phenotype, increased tumor cell multipotency, and malignancy (3). In the absence of *IDH1* point mutations, de novo GBMs are characterized by transcriptional up-regulation of wild-type (WT) IDH1. Genetic and pharmacological inactivation of WT IDH1 decreases GBM cell growth, promotes a more differentiated tumor cell state, increases apoptosis in response to radiation (4) and targeted therapies (5), and prolongs survival of animal subjects bearing patient-derived xenografts (PDXs) (5). On molecular levels, IDH1 inhibition reduces α KG and NADPH levels, which is paralleled by deficient carbon flux from glucose or acetate into lipids, exhaustion of reduced glutathione, increased levels of reactive oxygen species (ROS), and enhanced histone methylation and differentiation marker expression (5).

With defined roles for IDH1 and IDH2 in cancer progression evolving, our understanding of how IDH3 affects metabolic adaptation and tumorigenesis can reasonably be described as rudimentary. IDH3 catalyzes an irreversible and rate-limiting step of the TCA cycle (6), which is tightly regulated through substrate availability (ICT, NAD⁺, and Mg²⁺/Mn²⁺), product inhibition [NADH (reduced form of NAD⁺) and α KG], and competitive feedback inhibition [adenosine 5'-triphosphate (ATP)], to avoid unnecessary depletion of ICT and accumulation of α KG (7, 8). Reflecting its central role within the TCA cycle, down-regulation of IDH3 α , the catalytic subunit of the IDH3 heterotetramer (9), promotes transformation of fibroblasts into cancer-associated fibroblasts by inducing a switch from oxidative phosphorylation to glycolysis (10). Diminished IDH3 activity results in reduced α KG to fumarate and succinate ratio, which, in turn, inhibits prolyl hydroxylase domain-containing protein 2 (PHD2), promotes hypoxia-inducible factor 1 α (HIF1 α)-dependent up-regulation of glycolytic enzymes, and dampens oxidative phosphorylation (10). In contrast, in cervical epithelial adenocarcinoma cells and derivative explants, down-regulation of IDH3 α increases α KG levels, leading to HIF1 α inactivation and inhibition of tumor progression (11). In support of IDH3 α protumorigenic effect, IDH3 α expression correlates with poor postoperative overall survival of lung and breast cancer patients, pointing to IDH3 α as a putative cancer therapeutic target (11).

¹Ken and Ruth Davee Department of Neurology, The Northwestern Brain Tumor Institute, The Robert H. Lurie Comprehensive Cancer Center, Northwestern University, 303 East Superior, Chicago, IL 60611, USA. ²International Institute for Nanotechnology, Northwestern University, 2145 Sheridan Road, Evanston, IL 60208, USA. ³Department of Pharmacology and Cancer Biology, Duke University School of Medicine, Durham, NC 27710, USA. ⁴Preventive Medicine, Health and Biomedical Informatics, Feinberg School of Medicine, The Robert H. Lurie Comprehensive Cancer Center, Northwestern University, Chicago, IL 60611, USA. ⁵Metabolomics Core Facility of Robert H. Lurie Comprehensive Cancer Center, Northwestern University Feinberg School of Medicine, Chicago, IL 60611, USA. ⁶Department of Chemical and Biological Engineering, Northwestern University, Evanston, IL 60208, USA. ⁷Department of Medicine, Northwestern University Feinberg School of Medicine, Chicago, IL 60615, USA. ⁸Department of Neurological Surgery, Northwestern University Feinberg School of Medicine, Chicago, IL 60611, USA. ⁹Department of Pathology, Northwestern University Feinberg School of Medicine, Chicago, IL 60615, USA.

*Corresponding author. Email: a-stegh@northwestern.edu

In this study, we investigated whether IDH3 activity is regulated in GBM and whether this regulation, through mitochondrial and extramitochondrial metabolic rewiring of cancer cells, affects the tumor biologic properties of GBM. Using tissue microarray (TMA), gain- and loss-of-function studies, in vivo tumor models, immunoprecipitation (IP)–mass spectrometry (MS), and metabolomic studies, we demonstrate that IDH3 α is overexpressed in GBM compared to normal brain tissue and promotes orthotopic xenograft progression. In addition to IDH3's canonical function in regulating TCA cycle turnover and controlling mitochondrial energy metabolism, we found that IDH3 α , by colocalizing and interacting with cytosolic serine hydroxymethyltransferase (cSHMT), regulates one-carbon metabolism, a central metabolic pathway, which, via activation and transfer of one-carbon units, modulates pyrimidine synthesis as well as DNA methylation. Loss of IDH3 α function results in an increase in the methyl group donor *S*-adenosyl methionine (SAM) and DNA methylation while decreasing nucleotide availability during DNA replication and cellular growth. These studies point to IDH3 α -induced metabolic adaptation as a novel therapeutic point of intervention to halt GBM progression.

RESULTS

IDH3 α is overexpressed in GBM

In contrast to its paralogs IDH1 and IDH2, genomic sequencing studies revealed that IDH3 α , IDH3 β , and IDH3 γ subunits are not mutated in GBM (12). Analysis of the Ivy Glioblastoma Atlas Project (Ivy GAP) database, which contains RNA sequencing (RNA-seq) data from 10 regionally microdissected GBM tumors (<http://glioblastoma.alleninstitute.org/>) (13), revealed enrichment of IDH3 α and, to a lesser degree, IDH3 β and IDH3 γ transcript levels in cells of the leading edge and infiltrating tumor region when compared to the tumor center (Fig. 1A). Immunohistochemical (IHC) analysis of IDH3 α protein on TMA using a target-specific antibody (fig. S1A), followed by semiquantitative evaluation of protein expression by light microscopy (Fig. 1B), revealed that IDH3 α protein is elevated within the glioma tumor core compared to glial cells within normal brain tissue (Fig. 1C), irrespective of glioma grade (fig. S1B), and showed most robust expression within the GBM leading edge (Fig. 1, B and C). Notably, in silico analysis of The Cancer Genome Atlas (TCGA) expression profiles (14) found reduced IDH3 α , IDH3 β , and IDH3 γ transcripts in bulk tumor when compared to normal brain elements (5). Analysis of IDH3 α protein expression profiles within normal brain tissue, however, demonstrated high expression of IDH3 α in neurons (fig. S1C), prompting the more detailed comparative analysis of IDH3 α protein expression in cells of glial origin in normal brain versus GBM tumor cells presented here. In addition to mitochondrial distribution observed, which is consistent with well-described functions of IDH3 α within the mitochondrial TCA cycle (6), IDH3 α staining was also found to be associated with the tumor cell nucleus, as determined by confocal immunofluorescence (IF) microscopy on tumor sections (fig. S1D). Further, IDH3 α was also found in the tumor-associated endothelium, but not in the endothelium of normal brain tissue, with 0 of 8 normal cortex samples versus 12 of 12 GBM samples positive for IDH3 α endothelial cell staining (fig. S1, E and F). Together, these observations suggest that GBMs are characterized by elevated IDH3 α expression, with substantial IDH3 α expression detectable in peripheral tumor cells and tumor-associated endothelial cells.

IDH3 α promotes GBM progression

To determine whether IDH3 α can regulate in vivo GBM tumor progression, we generated a series of IDH3 α gain- and loss-of-function cell culture and derivative orthotopic xenograft model systems using minimally transformed cortical astrocytes [normal human astrocytes (NHAs)] and patient-derived glioma-initiating cells (GICs). Suppression of IDH3 α expression in luciferase-labeled NHAs via CRISPR-Cas9 genome editing (Fig. 2A) robustly decreased cellular growth (Fig. 2B). Animal subjects engrafted with IDH3 α -deficient NHAs showed reduced intracranial GBM tumor progression (Fig. 2, C and D). Antitumor effect as a result of IDH3 α deficiency was significantly antagonized by stable reexpression of IDH3 α in IDH3 α knockout (KO) NHAs (fig. S2A). Reduced bioluminescence of IDH3 α -deficient grafts translated into increased survival when compared to control explants (Fig. 2E). Histopathological analysis of sections from resected mouse brains revealed that IDH3 α KO was associated with a phenotypic shift from grade IV to grade III malignancy (Fig. 2F), reduced intratumoral proliferation as evidenced by diminished intratumoral mitoses (Fig. 2G), and reduced tumor cell invasion (fig. S2B). Control NHAs showed robust in vivo growth within the mouse cerebrum, including extensive invasion through the parenchyma into the leptomeningeal space (fig. S2B, a and b), while isogenic NHA tumors with IDH3 α KO were characterized by greatly attenuated growth in the cerebrum but were still capable of growth within the leptomeninges (fig. S2B, c to f). Enhanced migratory and invasive properties of IDH3 α expression were confirmed in primary human cerebral microvascular endothelial cells ectopically expressing IDH3 α protein (fig. S2, C and D). Similar to CRISPR-Cas9-mediated gene KO in NHAs, short hairpin RNA (shRNA)-mediated silencing of IDH3 α expression in patient-derived GICs (Fig. 2H) resulted in reduced GBM progression (Fig. 2, I and J) and improved animal subject survival (Fig. 2K). Correspondingly, in a gain-of-function approach, animal subjects engrafted with IDH3 α -overexpressing GICs (Fig. 2L) showed accelerated intracranial tumor progression (Fig. 2, M and N) and reduced survival when compared to vector controls (Fig. 2O). These data support GBM tumor-promoting activities of IDH3 α in physiologically relevant gain- and loss-of-function mouse models in vivo and suggest that IDH3 α inactivation reduces GBM progression and grade.

IDH3 α regulates TCA cycle turnover and glycolytic rates

IDH3 α catalyzes a rate-limiting, tightly controlled enzymatic reaction of the TCA cycle, which represents one of the most central metabolic pathways controlling cellular energy metabolism (15). To molecularly define IDH3 α protumor effect, we determined the metabolic alterations provoked by gain or loss of IDH3 α through MS-based metabolomic profiling (see table S1 for global metabolic changes comparing IDH3 α WT versus KO NHAs, and NHAs expressing vector control versus NHAs engineered to ectopically express IDH3 α). For all studies described below, logarithmically growing cells were harvested and subjected to ultraperformance liquid chromatography (UPLC)–MS/MS. To account for the different growth rates of control versus IDH3 α -modified NHAs, we confirmed identical numbers of viable cells by trypan blue exclusion and hemocytometer counting. Consistent with a central role of IDH3 α governing TCA cycle turnover, TCA cycle intermediates upstream of the IDH3-catalyzed reaction, i.e., citrate and ICT, were increased up to 50-fold in IDH3 α -deficient NHAs compared to control cells and, correspondingly, were decreased in NHAs engineered to stably express

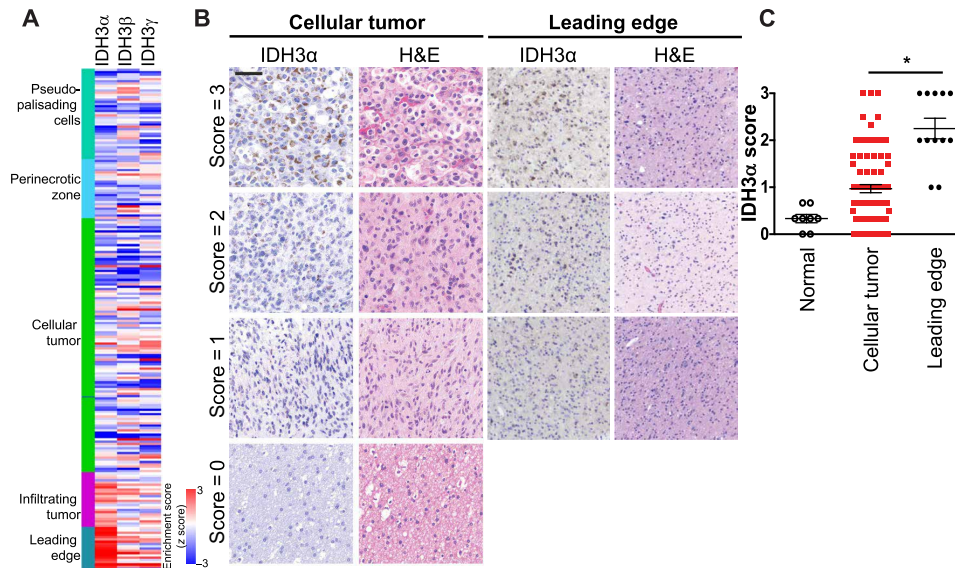


Fig. 1. IDH3 α expression is elevated in human-derived gliomas. (A) IDH3 α , IDH3 β , and IDH3 γ mRNA expression as determined by RNA-seq of 122 RNA samples from 10 regionally dissected GBM tumors (obtained from the Ivy GAP, <http://glioblastoma.alleninstitute.org/>). (B) Representative images of IDH3 α IHC stainings with different grading scores. Scale bar, 50 μ m. H&E, hematoxylin and eosin. (C) TMAs of GBM patient tumor samples, obtained from the University of Kentucky, and GBM tissue blocks containing tumor tissue of the leading edge were stained with IDH3 α antibody, and expression was quantified in glial cells of nontumor brain versus GBM tumor cells. * $P = 0.03$, one-way analysis of variance (ANOVA); $n = 8$ for nontumor, $n = 87$ for cellular tumor samples, $n = 12$ for leading edge.

an IDH3 α transgene (Fig. 3A). A smaller yet notable accumulation of the later intermediates (i.e., succinate, fumarate, and malate) downstream of IDH3 further suggests that overall TCA cycle activity is low in IDH3 α -deficient NHAs (Fig. 3A). Targeted metabolomic tracer studies using uniformly ^{13}C -labeled glucose and LC-MS confirmed decreased TCA flux in IDH3 α -deficient cells (Fig. 3B), resulting in a decreased αKG to succinate and fumarate ratio (Fig. 3C). As a consequence of reduced TCA cycle turnover in IDH3 α -deficient NHAs, oxygen consumption rates are diminished (Fig. 3D) and aerobic glycolysis increased (Fig. 3E), as evidenced by lower levels of glycolysis intermediates, including glucose, glucose-6-phosphate, pyruvate, coenzyme A (CoA), phosphoenolpyruvic acid, 3-phosphoglycerate (3PG), and 2PG (see also table S1), and increased glycolytic carbon flux (Fig. 3F). Together, these metabolomic and functional studies demonstrate that ablation of IDH3 α is associated with a metabolic switch from oxidative phosphorylation to glycolysis.

IDH3 α interacts with cSHMT during S phase

Consistent with an evolutionarily conserved monopartite nuclear localization signal (NLS) at amino acid position 124 of the IDH3 α polypeptide (GASKRIAFAF), our IF studies on tumor sections (fig. S1D), together with previous studies (16, 17), demonstrate (peri-)nuclear distribution of the IDH3 α subunit in a subset of tumor cells and suggest IDH3 α extramitochondrial activity. To assess subcellular localization of IDH3 α in GBM tumor cells, and to determine whether IDH3 α intracellular distribution is controlled by the cell cycle, cell fractionation into nuclear and extranuclear fractions, the latter containing cytoplasmic and heavy membrane components, revealed predominant extranuclear localization of IDH3 α , with nuclear localization of IDH3 α evident in S phase-arrested glioma cells (Fig. 4, A and B). Confocal IF microscopy confirmed predominant

mitochondrial localization of IDH3 α in unsynchronized cells (Fig. 4C, a and b, and fig. S3A), and a more diffuse cytosolic distribution (Fig. 4C, c, and fig. S3A) and association with the periphery of the cell nucleus in S phase-arrested cells (Fig. 4C, c, and fig. S3B). To determine the molecular function of cell cycle-induced extramitochondrial IDH3 α , we defined the IDH3 α interactome using IP-MS studies in patient-derived GICs, expressing a scrambled or an IDH3 α -targeting shRNA. Peptides derived from four proteins were reproducibly detected in shScr-expressing GICs upon IDH3 α -specific pull-down, but not in immunoglobulin G (IgG) isotype-matched control precipitates or in GICs stably expressing shRNA targeted to IDH3 α (Fig. 4, D and E). Among the four candidates, cSHMT was the only IDH3 α interactor that coprecipitated with IDH3 α in all transformed GBM cell lines, patient-derived GICs, and NHAs. cSHMT, an integral enzyme involved in one-carbon metabolism, is part of a multienzyme complex, which consists of cSHMT, thymidylate synthase (TYMS), and dihydrofolate reductase (DHFR). The complex, which regulates thymidylate biosynthesis, localizes to the cytosol, with suggestions that it can translocate to the cell nucleus during S phase (18). cSHMT catalyzes the rate-limiting step and serves as a scaffold essential for complex formation. Within the cell nucleus, the complex can associate with the nuclear lamina, can localize at sites of DNA replication, and is associated with components of the DNA replication machinery (18, 19). Reciprocal IPs following WB analysis using both IDH3 α and cSHMT precipitating antibodies validated the IDH3 α -cSHMT interaction (Fig. 4F). While cell cycle distribution did not affect total protein levels of IDH3 α and cSHMT, as evidenced by WB analysis of whole-cell lysate derived from unsynchronized and S phase-arrested NHAs (fig. S3C), confocal IF microscopy analysis confirmed colocalization of IDH3 α and cSHMT in the cytosol (fig. S3A) and at the nuclear envelope in S phase-arrested cells (fig. S3B). In addition to cytoplasmic and

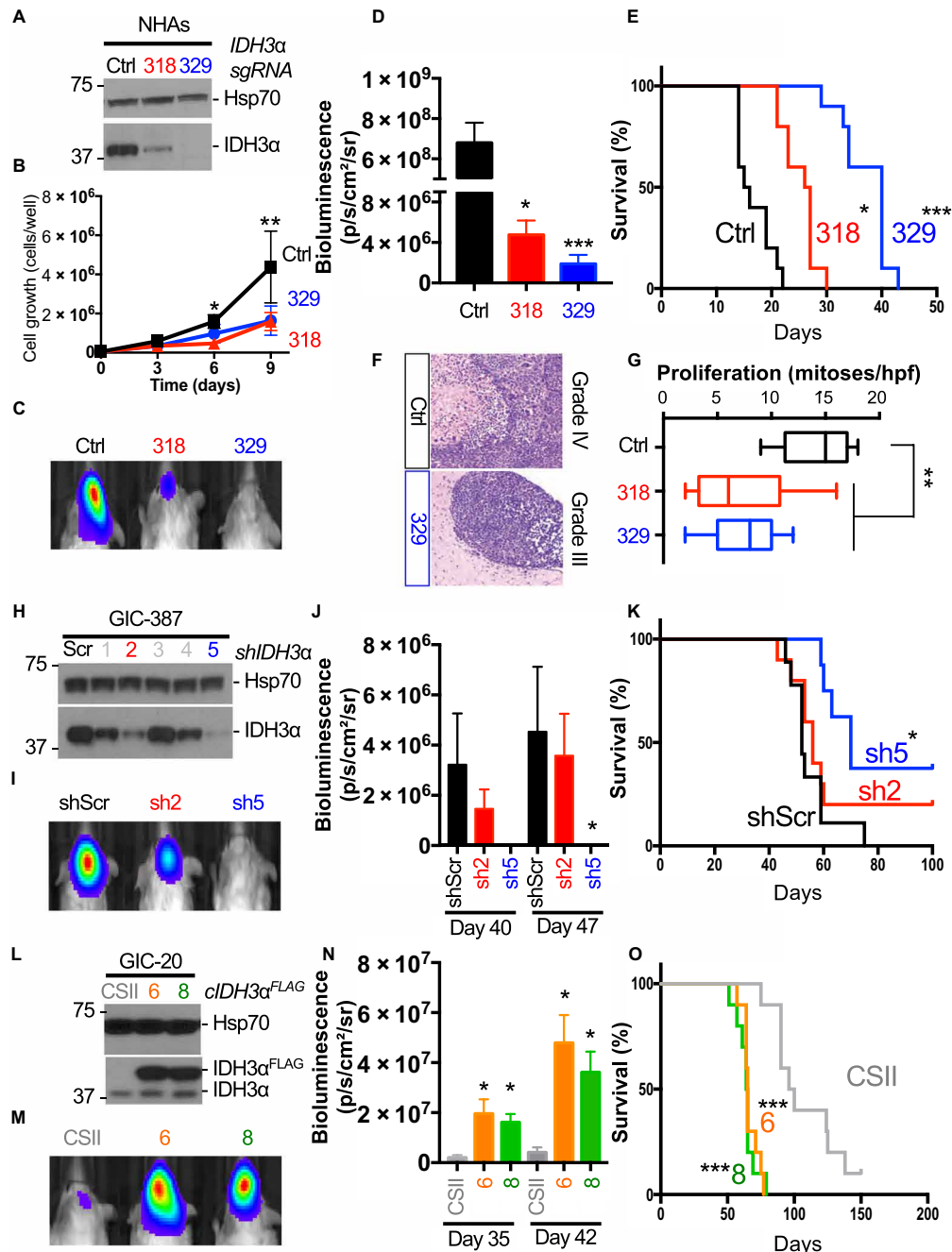


Fig. 2. IDH3α regulates GBM progression in vivo. (A to G) IDH3α ablation reduces glioma tumor progression. (A) Western blot (WB) showing IDH3α expression in CRISPR-Cas9-modified NHAs; NHAs were transfected with a scrambled single-guide RNA (sgRNA) (Ctrl) and two different IDH3α-targeting sgRNAs, i.e., sgRNA-318 and sgRNA-329. Hsp70 is shown as a control. (B) In vitro cell growth curves of IDH3α WT and IDH3α KO NHAs. Cells were counted every 3 days using trypan blue and an automated cell counter. Means ± SD are shown; $n = 3$; $*P < 0.05$, $***P < 0.005$. (C) Representative in vivo imaging system (IVIS) images of brain tumor-bearing mice, demonstrating reduced bioluminescence in IDH3α KO tumor-bearing mice compared to the WT control. (D) Quantification of bioluminescence signal at day 13 after intracranial cell inoculation. Means ± SEM are shown; $*P < 0.05$, $***P < 0.0005$; $n = 10$ per group. (E) Kaplan-Meier survival curves of mice orthotopically implanted with IDH3α WT or KO NHAs. $*P < 0.05$, $***P < 0.0005$; $n = 10$ per group. (F) Representative H&E stainings of tumor sections from IDH3α WT and KO tumors. (G) Number of mitoses in tumors per high-power field (hpf): two tumors per group and eight slices per tumor. $***P < 0.005$, one-way ANOVA. (H to K) RNA interference (RNAi)-mediated IDH3α knockdown (KD) reduces tumor progression in PDX mice. (H) WB analysis for IDH3α in different GIC clones modified for stable IDH3α KD. Hsp70 is shown as a loading control. (I) Representative IVIS images of PDX-bearing mice. (J) Quantification of bioluminescence signal 40 and 47 days after tumor implantation. $*P < 0.05$; $n = 8$ per group. (K) Kaplan-Meier survival curves of mice intracranially injected with GICs modified for IDH3α stable KD in comparison to PDX tumors expressing a scrambled control shRNA. $*P < 0.05$; $n = 8$ per group. (L to O) IDH3α overexpression in GICs promotes GBM tumor progression. (L) WB analysis for endogenous and FLAG epitope-tagged IDH3α. Hsp70 is shown as a loading control. (M) Representative IVIS images of mice harboring vector (CSII) control and IDH3α^{FLAG}-expressing brain tumors. (N) Quantification of bioluminescence signal in mice 35 and 42 days after cell inoculation. $*P < 0.05$; $n = 10$ per group. (O) Kaplan-Meier survival curves of mice intracranially injected with CSII vector control and IDH3α-overexpressing GICs. $***P < 0.0005$; $n = 10$ per group.

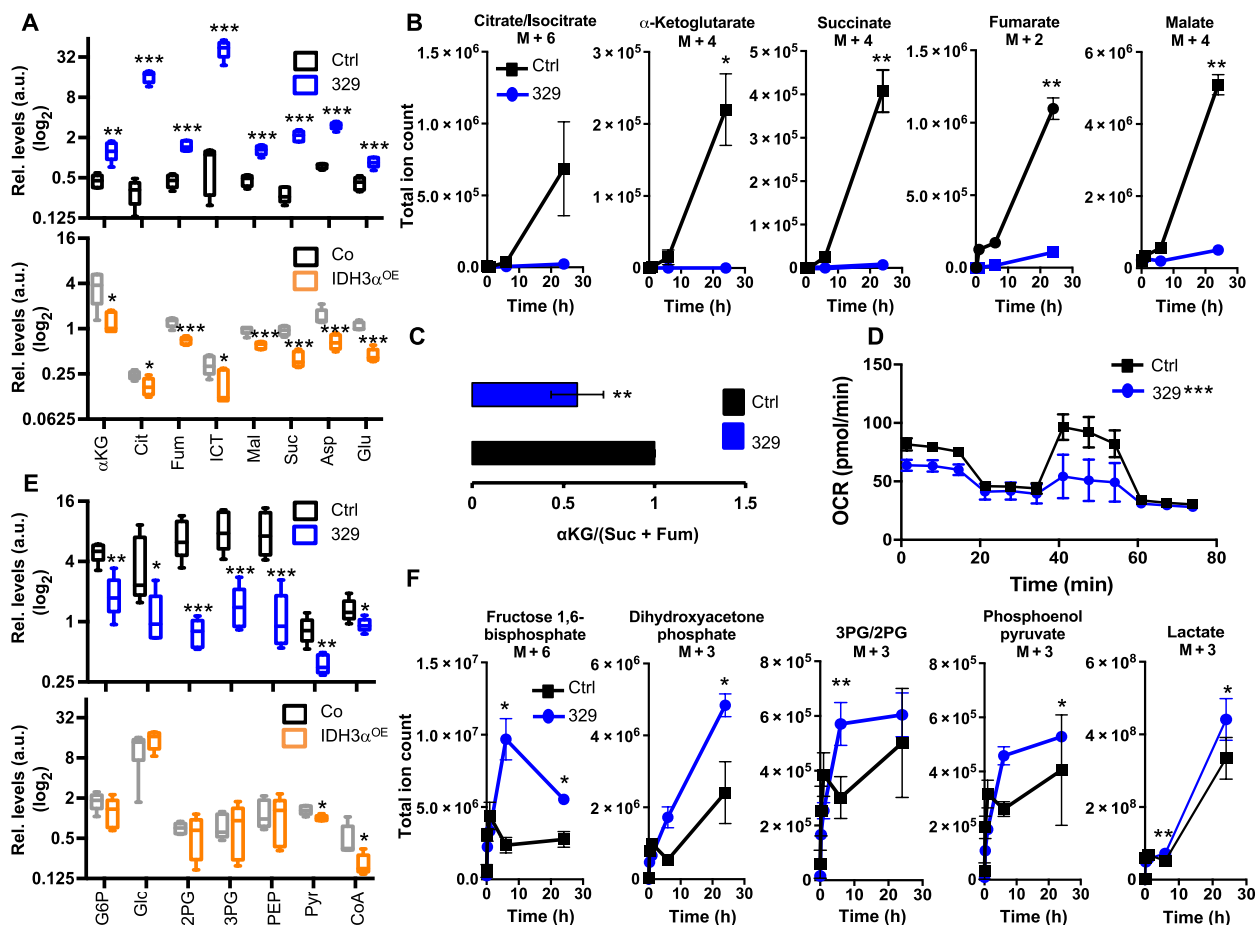


Fig. 3. IDH3 α modulates TCA cycle and glycolysis. (A) Levels of TCA cycle intermediates as determined by LC-MS. Significance was determined by Welch's two-sample *t* test; **P* < 0.05, ****P* < 0.005, *****P* < 0.0005; *n* = 5. a.u., arbitrary units; OE, overexpressing; Cit, citrate; Fum, fumarate; Mal, malate; Suc, succinate. (B) Total ion counts of ¹³C-labeled TCA metabolites. Samples were analyzed at 0 hours, 15 min, 1 hour, 6 hours, and 24 hours after addition of uniformly ¹³C-labeled glucose. Means \pm SD are plotted; **P* < 0.05; *n* = 3 per time point. (C) Ratio of α KG to succinate and fumarate. Means \pm SD are shown. (D) Changes in the oxygen consumption rate (OCR) in IDH3 α WT versus IDH3 α KO cells. The concentrations of oligomycin, carbonyl cyanide *m*-chlorophenyl hydrazone (CCCP), antimycin A, and rotenone were 2, 10, 2, and 2 μ M, respectively. Each data point represents means \pm SD and is representative of 18 technical replicates; ****P* = 0.0048; *n* = 3. (E) Levels of glycolysis intermediates as determined by LC-MS, significance determined by Welch's two-sample *t* test; **P* < 0.05, ****P* < 0.005, *****P* < 0.0005; *n* = 5. PEP, phosphoenolpyruvate. (F) Total ion counts of ¹³C-labeled glycolysis metabolites. Samples were analyzed at 0 hours, 15 min, 1 hour, 6 hours, and 24 hours after addition of uniformly ¹³C-labeled glucose. Means \pm SD are plotted; **P* < 0.05; *n* = 3 per time point.

laminar distributions, a smaller fraction of S phase-arrested NHAs showed a more pronounced nucleoplasmic pool of IDH3 α , which did not show colocalization with cSHMT (insets in fig. S3A). Figure S3D shows a quantification of IDH3 α and cSHMT colocalization, using a macro that created a mask for cSHMT intracellular distribution, and determined the percentage of IDH3 α staining covered by the cSHMT mask, relative to total IDH3 α .

IDH3 α regulates nucleotide biosynthesis and DNA methylation

cSHMT controls one-carbon metabolism, a central metabolic pathway, which uses folate molecules as carriers of one-carbon units, to support nucleotide synthesis, as well as DNA and protein methylation (20). Tetrahydrofolate (THF), the biologically active form of folate, interconverts bound one-carbon units between different oxidation states, i.e., *N*⁵, *N*¹⁰-methylene-THF, *N*⁵-methyl-THF, and *N*¹⁰-formyl-THF, each supporting distinct biosynthetic functions (fig. S4). *N*⁵, *N*¹⁰-methylene-THF drives thymidine synthesis; *N*¹⁰-

formyl-THF supports de novo purine synthesis and can be fully oxidized, generating CO₂ and NADPH (21); and *N*⁵-methyl-THF is channeled into the methionine salvage pathway to produce the reactive methyl donor SAM and to methylate DNA and protein (fig. S4). cSHMT appropriates *N*⁵, *N*¹⁰-methylene-THF between nucleotide and SAM biosynthesis, with cSHMT overexpression increasing nucleotide and decreasing SAM availability (22, 23). Therefore, using LC-MS metabolite profiling and targeted flux studies, together with metabolite rescue and DNA methylation experiments, we assessed whether and to what extent IDH3 α regulates cSHMT-controlled nucleotide biosynthesis versus methionine salvage pathway utilization. IDH3 α -deficient NHAs showed increased ¹³C label incorporation into both serine and glycine compared to WT cultures (Fig. 5A). This flux increase likely results from increased glycolytic activity, with the glycolytic intermediate 3PG being diverted toward the serine synthesis pathway (fig. S4) (24). Similarly, IDH3 α ablation resulted in increased flux into the pentose phosphate pathway (PPP; Fig. 5B), as the glycolytic intermediate glucose-6-phosphate can be

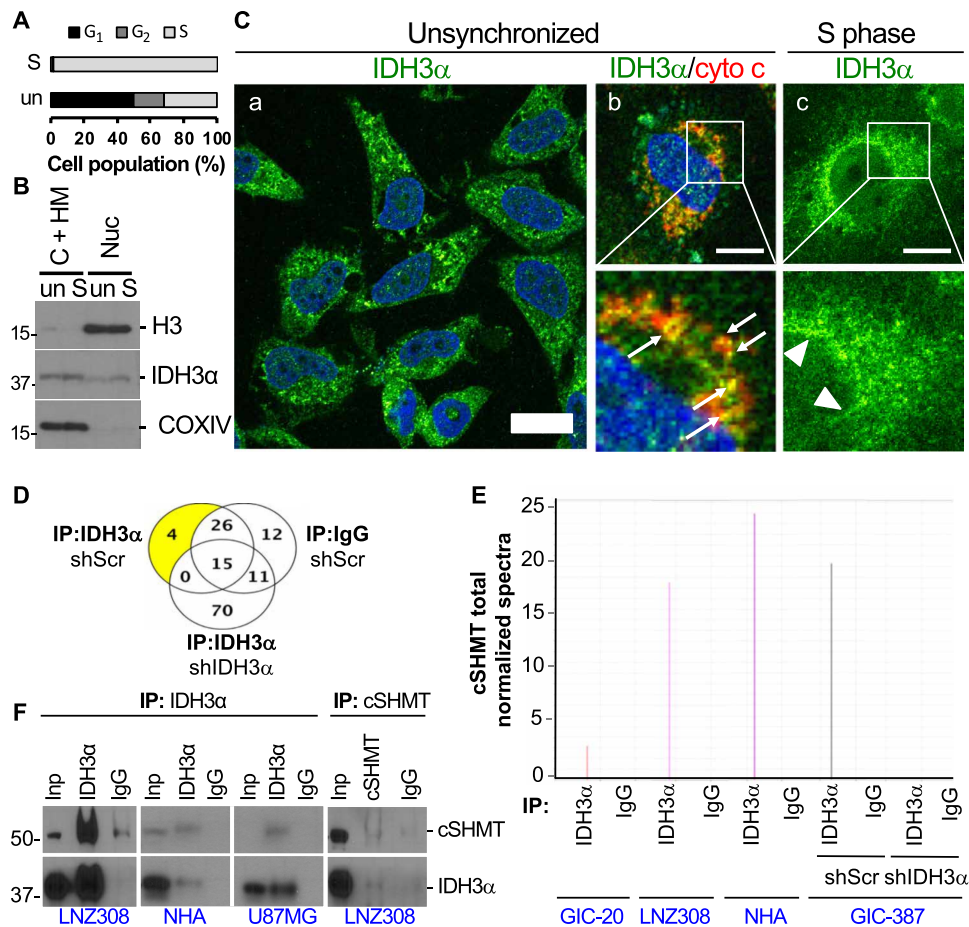


Fig. 4. IDH3 α interacts with cSHMT during S phase at the nuclear lamina. (A) Cell cycle distribution in unsynchronized and S phase-arrested NHA cells as indicated by propidium iodide staining and flow cytometry-based quantification of G_1 , G_2 -M, and S phase content. un, unsynchronized; S, synchronized. (B) WB analysis of IDH3 α in heavy membrane (HM) and cytosolic (C) compared to nuclear (Nuc) fractions. Histone H3 and cytochrome c oxidase subunit IV (COXIV) are shown as nuclear and mitochondrial markers, respectively. (C) Confocal IF images of unsynchronized (a and b) and S phase-arrested NHAs (c) stained for IDH3 α (green), cytochrome c (cyto c; red), and DNA (Hoechst; blue). Scale bars, 20 μ m (a), 14 μ m (b), and 22 μ m (c). Arrows point to IDH3 α colocalizing with cytochrome c, and arrowheads point to IDH3 α associated with the nuclear lamina. (D) Venn diagram illustrating IDH3 α co-immunoprecipitated proteins using IgG control or IDH3 α -specific antibodies in shScr- and shIDH3 α -expressing GICs. (E) Bar graph illustrating total normalized cSHMT spectra in IgG and IDH3 α immunoprecipitates in the indicated cell lines. (F) IP-WB analysis of IDH3 α and cSHMT validates the IDH3 α -cSHMT complex.

channeled into the PPP to generate ribose-5-phosphate, a precursor for nucleotide biosynthesis (fig. S4). As a result of increased PPP utilization, ^{13}C label incorporation into uridine 5'-monophosphate (UMP) is elevated (Fig. 5C), yet thymidine 5'-monophosphate (TMP) levels, together with other pyrimidine biosynthesis intermediates, i.e., uridine, uracil, thymidine, thymine, and TMP, accumulated in IDH3 α -deficient cells, as determined by LC-MS (Fig. 5D). These results are consistent with reduced pyrimidine pathway activity that leads to an accumulation of intermediates. Mirroring the accumulation of intermediates in IDH3 α -deficient cells, NHA cultures engineered to ectopically express IDH3 α showed a corresponding decrease in pathway intermediates (Fig. 5D). While decreasing pyrimidine biosynthesis activity (Fig. 5D), IDH3 α deficiency augmented the SAM/SAH (S-adenosyl homocysteine) ratio and reduced the methionine pathway intermediates N^5 -methyl-THF and homocysteine (HCY), indicative of increased metabolic flux through the methionine salvage pathway (Fig. 5, E to G). SAM supports methylation of lipids, DNA, RNA, metabolites, and proteins (25). While

MS did not detect robust changes in global levels of histone methylation marks (fig. S5A), IDH3 α KO NHAs compared to IDH3 α WT cells showed increased levels of DNA methylation, as determined by quantification of global 5-methylcytosine (5mC) levels using dot blot and enzyme-linked immunosorbent assay (ELISA) assays (fig. S5, B to D). Consistently, labeling of NHA cultures with ^{13}C serine and quantification of label incorporation into 5mC revealed higher ratios of 5mC + 1/5mC in IDH3 α -deficient versus WT cells (Fig. 5H). Because of reduced α KG to fumarate and succinate ratio, increased DNA methylation in IDH3 α KO NHAs could be due to reduced activity of ten-eleven translocation methylcytosine (TET) dioxygenases, which are inhibited by succinate and fumarate (26). TET enzymes catalyze the conversion of 5mC to 5-hydroxymethylcytosine (5hmC), considered to be the initial step of DNA demethylation (26). To address the potential contribution of α KG-dependent TET enzymes to the hypermethylation phenotype in IDH3 α -deficient NHAs, we quantified levels of 5hmC in IDH3 α WT versus KO NHAs by colorimetric ELISA. As shown in fig. S5E, we did not observe a

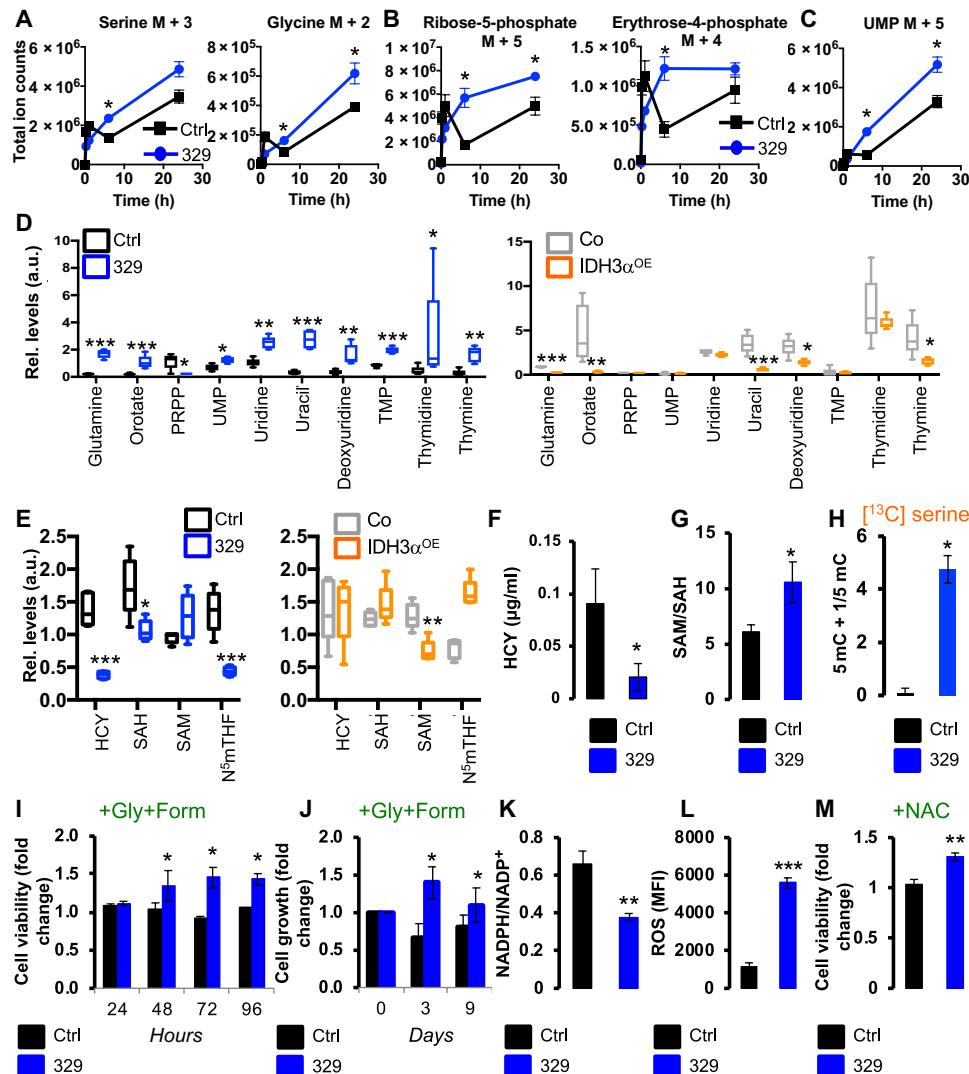


Fig. 5. IDH3 α modulates one-carbon metabolism. (A to C) Total ion counts of uniformly ¹³C-labeled serine and glycine (A), PPP pathway metabolites (B), and UMP (C) in NHAs with IDH3 α loss of function. Samples were taken at 0-hour, 15-min, 1-hour, 6-hour, and 24-hour time points. Means \pm SD are shown; * P < 0.05; n = 3 per time point. (D and E) Histograms showing changes in pyrimidine (D) and methionine (E) metabolite levels in NHAs with IDH3 α loss or gain of function as identified by LC-MS. Significance was determined by Welch's two-sample t test; * P < 0.05, ** P < 0.005, *** P < 0.0005; n = 5. N⁵mTHF, N⁵-methyl-THF. (F) HCY levels in control versus IDH3 α KO NHAs as determined by ELISA. Means \pm SD are shown; * P < 0.05; n = 3. (G) Ratio of intercellular SAM/SAH in control WT versus IDH3 α KO NHAs. Means \pm SD are shown; * P < 0.05; n = 3. (H) ¹³C label incorporation into 5'-mC as determined in WT and IDH3 α KO NHAs fed with ¹³C serine. (I and J) Relative viability as assessed by 3-(4,5-dimethylthiazol-2-yl)-2,5-diphenyltetrazolium bromide MTT assay (I) and growth (J) of IDH3 α WT versus IDH3 α KO NHAs treated with 1 mM formate (Form) and 0.4 mM glycine (Gly) compared to cultures treated with glycine only. Data are expressed as relative to day 0. Means \pm SD are shown; * P < 0.05; n = 3. (K) Levels of intracellular NADPH/NADP⁺ in IDH3 α WT versus IDH3 α KO NHAs. Means \pm SD are shown; ** P < 0.005; n = 4. (L) Relative ROS levels in IDH3 α WT versus IDH3 α KO. Means \pm SD are shown; *** P < 0.0005; n = 3. MFI, mean fluorescence intensity. (M) Relative cell viability of WT versus IDH3 α KO NHAs after treatment with 0.5 mM NAC or vehicle for 48 hours. Means \pm SD are shown; ** P < 0.005; n = 3.

difference in 5hmC levels between WT and KO cells. Furthermore, addition of formate to replenish THF levels, but not the addition of cell-permeable dimethyl- α KG, restored 5mC levels to those observed in IDH3 α -proficient NHAs (fig. S5, C and D), suggesting that the contribution of α KG-dependent TET enzymes to the observed DNA hypermethylation phenotype in IDH3 α KO NHAs is minor.

To evaluate whether and to what extent differential methylation in IDH3 α -deficient versus IDH3 α -proficient NHAs controls gene expression, we performed integrative RNA-seq and methylation profiling experiments. RNA-seq analysis identified 8711 differentially

expressed genes, with differential expression defined at a threshold of false discovery rate (FDR) = 0.05 and an absolute log fold change > 1 (fig. S6, A and B). Through integrative analysis of expression and methylation data, we determined that, out of the 8711 differentially expressed genes, expression of 3084 genes correlated with their CpG methylation status (fig. S6C). Expectedly, correlation was primarily observed for CpG sites located within island and shores, in comparison to shelf and open sea. Pathway enrichment analysis of genes with correlation between gene expression and methylation pointed to adenosine 3',5'-monophosphate (cAMP)-mediated signaling and the regulation of epithelial-to-mesenchymal transition

(EMT) as key pathways deregulated through methylation-driven expression changes upon IDH3 α deletion (fig. S6D). Notably, while the higher number of hypermethylated relative to hypomethylated CpGs revealed an overall global increase in DNA methylation in IDH3 α KO cells (fig. S6E), confirming our 5mC dot blot analysis (Fig. 5H), hypermethylated CpGs in IDH3 α KO cells were enriched in open sea regions (fig. S6F). Together with the overall modest overlap between differentially methylated genes with those showing differential expression, these data suggest that IDH3 α -controlled gene regulation may occur through additional mechanisms other than methylation of promoter-proximal regulatory elements (see Discussion below).

In further support of an IDH3 α -cSHMT signaling axis, pathway enrichment analysis of the IDH3 α -controlled metabolome confirmed folate one-carbon metabolism as a high-priority metabolic pathway modulated by IDH3 α (enrichment scores of 5.75 in KO versus WT and 3.2 in IDH3 α overexpressing versus WT NHAs, with a *P* value cutoff of 0.001). Correspondingly, addition of formate to replenish THF levels selectively increased viability and growth of IDH3 α KO cells, compared to WT NHAs (Fig. 5, I and J), and restored levels of 5mC to those observed in IDH3 α -proficient cells (fig. S5B). Furthermore, as NADPH is used by the folate pathway and by the conversion of serine to sphingolipids (27, 28), IDH3 α deficiency resulted in decreased NADPH levels (Fig. 5K) and increased levels of ROS (Fig. 5L), and addition of the ROS scavenger *N*-acetylcysteine (NAC) increased viability of IDH3 α KO compared to WT NHAs (Fig. 5M). Furthermore, treatment of IDH3 α -deficient cells with methotrexate (MTX), an inhibitor of TYMS and DHFR (29, 30), which promotes apoptosis through ROS generation (31), reduced cell viability in IDH3 α KO NHAs compared to WT control cells (fig. S7A), while IDH3 α -overexpressing NHAs were protected against MTX cytotoxic effect (fig. S7B). Analysis of effector caspase activation confirmed increased levels of apoptosis in IDH3 α -deficient cells when compared to WT controls. Introduction of an IDH3 α complementary DNA (cDNA) into IDH3 α -deficient cells was able to rescue the proapoptotic phenotype of IDH3 α compromise (fig. S7C). These results suggest that IDH3 α loss through reduced cSHMT and thymidylate synthesis cooperates with antifolate therapy to promote apoptosis. To assess the relative contribution of mitochondrial versus extramitochondrial activity to IDH3 α antiapoptotic effect, we generated an IDH3 α protein that lacks the evolutionarily conserved mitochondrial targeting signal (Δ MTS; fig. S7D). Δ MTS-IDH3 α failed to colocalize with the mitochondrial marker cytochrome *c* (fig. S7E), yet fully retained enzymatic activity (fig. S7, F to H). When compared to full-length IDH3 α protein, Δ MTS-IDH3 α was even more active in blocking MTX-induced effector caspase activation (fig. S7I), suggesting that IDH3 α mitochondrial activity is dispensable for its antiapoptotic effect. Together, these data suggest that similar to cSHMT compromise (22, 23), IDH3 α loss of function impairs redox homeostasis and nucleotide biosynthesis while increasing the cellular methylation potential.

DISCUSSION

We demonstrated that IDH3 α protein is up-regulated in GBM tumor and, as shown in physiologically relevant CRISPR-Cas9 and RNAi loss of function, together with gain-of-function studies in orthotopic tumor models, promotes GBM progression. On molecular levels, IDH3 α ablation reduces TCA cycle turnover and shunts en-

ergy metabolism. In addition, IDH3 α affects one-carbon metabolism and regulates nucleotide production as well as DNA methylation through effect on cSHMT.

In contrast to its paralogs IDH1 and IDH2, genomic sequencing studies revealed that glioma-associated IDH3 α , IDH3 β , and IDH3 γ subunits are not mutated (12). We found that GBM tumor cells up-regulate IDH3 α mRNA and protein when compared to glial cells in normal brain, with IDH3 α abundance most prominent within the leading edge of GBM tumor specimens. Association with tumor cells of the leading edge was more evident for *IHD3A* mRNA compared to IDH3 α protein. These data suggest that IDH3 α expression may be regulated through additional mechanisms besides transcriptional control. Expectedly, because of TCA cycle and respiratory compromise, IDH3 α ablation triggered a compensatory metabolic shift to aerobic glycolysis and increased PPP utilization.

In addition to mitochondrial distribution of IDH3 α , our subcellular fractionation and IF studies revealed cell cycle-induced cytosolic and (peri-)nuclear localization of IDH3 α , the latter consistent with an evolutionarily conserved monopartite NLS at amino acid position 124 of the IDH3 α polypeptide (GASKRIAEFAF). This finding confirms previous proteomic analyses of isolated cancer cell nuclei and mitochondria, which demonstrated distribution of various TCA cycle enzymes, including IDH3 α , to both nucleus and mitochondria (16, 17). In particular, Nagaraj *et al.* (17) demonstrate that multiple TCA enzymes, including IDH3, localize to the cell nucleus while maintaining a mitochondrial pool during embryonic development. Enzymes associated with the cell nucleus are enzymatically active and, as part of the first half of the TCA cycle, contribute to metabolites, such as acetyl-CoA and α KG, which are essential for epigenetic control of gene expression and activation of the zygotic genome during preimplantation development (17). In glioma cells and NHAs, IDH3 α extramitochondrial localization was cell cycle dependent, as S phase-arrested cells showed predominant accumulation of IDH3 α in the cytosol and at the nuclear periphery. Here, IDH3 α colocalized and interacted with cSHMT, a rate-limiting enzyme of the *de novo* thymidylate synthesis pathway (18). cSHMT is a lamin-binding protein that serves as a scaffold protein required for the recruitment of TYMS and DHFR into a multienzyme complex in both cytosol and nucleus (18, 19). cSHMT, TYMS, and DHFR can translocate to the nucleus via posttranslational modification with the small ubiquitin-like modifier (19), can accumulate at the nuclear lamina during S and G₂-M phases, and, through cSHMT, interact with components of the DNA replication machinery to support *de novo* thymidylate synthesis at sites of DNA replication (18). During DNA replication, cSHMT appropriates N⁵, N¹⁰-methylene-THF between nucleotide synthesis and methionine salvage pathways (23). cSHMT compromise causes elevated levels of uracil in nuclear DNA and increased N⁵, N¹⁰-methylene-THF flux into the salvage methionine cycle, as evidenced by increased SAM levels (23), predisposing mice with heterozygous loss of cSHMT to neural tube defects (32). Similarly, reduced *de novo* thymidylate synthesis resulting from folate deficiency or antifolate treatment results in deoxyuridine misincorporation into mitochondrial DNA and nuclear DNA, leading to genome instability (33). Mirroring cSHMT compromise, IDH3 α deficiency caused accumulation of pyrimidine pathway intermediates and a decrease in total NADPH/NADP⁺ ratio. Despite increased PPP utilization in NHAs with IDH3 α compromise, PPP pathway activity was unable to compensate for increased NADPH consumption through the folate-methionine salvage pathway;

two NADPH molecules are generated by the PPP, while three NADPH molecules are consumed by the folate pathway in converting THF to N^5 -methyl-THF for the methionine pathway (fig. S4).

In further support of IDH3 α as a cSHMT interactor and modulator of the thymidylate synthesis pathway, levels of methionine salvage pathway intermediates, such as HCY and SAH, decreased, and SAM levels and associated DNA methylation increased. Addition of the THF precursor formate to IDH3 α KO NHA restored cell viability, suggesting that blunted one-carbon metabolism is central to the growth deficit in response to IDH3 α loss. We propose that blunted nucleotide biosynthesis, together with epigenetic silencing of potent growth and multipotency factors in response to IDH3 α loss of function, creates a unique metabolic vulnerability in highly proliferative cells, such as tumor cells, that decreases cellular viability, and cooperates with antifolate therapy, such as MTX, known to target the thymidylate pathway enzymes DHFR and TYMS, to promote programmed cell death.

cSHMT scaffold function rather than its enzymatic activity appears to be critical for de novo thymidylate biosynthesis (18). Neuroblastoma cells expressing a dominant-negative, enzymatically inactive cSHMT that retained lamin binding activity showed reduced incorporation of cSHMT-derived one-carbon units into the cytoplasmic methionine salvage pathway, while de novo thymidylate synthesis was not impaired (18). We propose that IDH3 α binds cSHMT in the cytosol, as indicated by colocalization of IDH3 α and cSHMT in the cytosol of S phase-arrested cells, and may aid in recruiting cSHMT to the nuclear lamina and, in so doing, enhances nucleotide biosynthesis to support unabated cancer cell growth. Genetic inactivation of IDH3 α , while impairing nucleotide biosynthesis and cellular growth, enhances the cellular methylation potential by increasing methionine salvage pathway utilization and the SAM/SAH ratio, resulting in DNA hypermethylation and the suppression of an oncogenic signature important for cellular growth and differentiation. In the presence of exogenous methionine, serine can contribute to de novo synthesis of ATP, which is required to convert methionine to SAM (fig. S4) (34). cSHMT-generated glycine, together with phosphoribosyl pyrophosphate (PRPP) and N^{10} -formyl-THF, which, in the absence of functional IDH3 α , does not significantly contribute to thymidylate synthesis, can enter the de novo ATP synthesis pathway. Therefore, the IDH3 α -cSHMT signaling axis may not only affect folate appropriation between nucleotide synthesis and methionine salvage pathways but also regulate DNA methylation through effect on de novo ATP production (fig. S4).

The interplay between altered cancer cell metabolism and epigenetic reprogramming has been well established. Aberrant expression or mutation of cancer-promoting genes causes alterations in metabolites that modify chromatin structure and gene expression, such as NAD^+ / $NADH$, flavin adenine dinucleotide (FAD^+), O-linked *N*-acetylglucosamine, free fatty acids, SAM, and acetyl-CoA (35). Aberrant expression of IDH3 α through effects on one-carbon metabolism affects the methylation potential of cells and, in so doing, regulates transcription of cancer-causing genes. Through integrative analysis of methylation array and RNA-seq data, followed by pathway enrichment analysis, we found that cAMP-mediated signaling and the regulation of EMT pathways were deregulated in the setting of IDH3 α deletion. With limited overlap between differentially methylated and differentially expressed genes, and the enrichment of hypermethylated CpG elements in IDH3 α KO NHAs within open sea regions, we anticipate that IDH3 α , by promoting DNA hyper-

methylation, regulates gene expression through additional mechanisms, e.g., by regulating the repetitive genome. A recent study found that loss of LKB1 (liver kinase B1) in the setting of KRAS mutation alters serine/glycine one-carbon metabolism in prostate cancer and affects DNA methylation of retrotransposon elements, which, upon methylation, were transcriptionally silenced (25).

Limitations of the current study relate to the determination of precise mechanisms of IDH3 α subcellular redistribution and to the elucidation of the binding interface between IDH3 α and cSHMT. Biophysical along with point mutation experiments, in future studies, will define the binding interface between IDH3 α and cSHMT. These studies will determine how the structures of both IDH3 α and cSHMT are altered upon complex formation and will define the precise mechanism of IDH3 α effect on cSHMT localization, activity, scaffold function, and thymidylate synthesis complex assembly.

Together, the identification of a noncanonical extramitochondrial function of IDH3 α suggests a previously unrecognized functional interplay between mitochondrial energy and one-carbon metabolism. Our study points to cancer-associated IDH3 α expression and IDH3 α -controlled one-carbon metabolism as novel metabolic vulnerabilities in GBM. While normal cells, such as cortical astrocytes, show reduced growth rates upon IDH3 α KD (relative cell confluence at 72 hours after cell plating: Ctrl, 6.5; IDH3 α KD, 4.6, as determined by IncuCyte analysis), we hypothesize that noncanonical function of IDH3 α , i.e., its interaction with cSHMT and the modulation of one-carbon metabolism, selectively occurs in rapidly dividing cells with high demand for nucleotide biosynthesis. We suggest that targeting the IDH3 α -cSHMT signaling axis via small molecules to disrupt their interaction may represent a novel therapeutic strategy for the treatment of GBM. As cancer cells depend on DNA synthesis to support unabated growth, multiple enzymes implicated in one-carbon metabolism are up-regulated in cancer, including TYMS, DHFR and SHMT2, and cSHMT (36). Our data point to IDH3 α overexpression as a means to regulate cSHMT function, and underscore the importance of therapeutic strategies to target components of the thymidylate pathway to halt GBM tumor progression.

MATERIALS AND METHODS

Experimental design

The objective of this study was to determine the role of IDH3 α in GBM progression. We investigated mRNA and protein expression of IDH3 subunits in GBM tumor specimens by analysis of RNA-Seq datasets together with IHC-TMAs. Gain- and loss-of-function explant models aimed to establish oncogenic function of IDH3 α in vivo, and mechanistic studies, using unbiased IP-MS, metabolic flux, and subsequent functional validation studies, evaluated the role of IDH3 α in mitochondrial and extramitochondrial metabolic pathways.

Cell culture

Patient-derived GIC-20 (gift from K. Aldape, University of Toronto) and GIC-387 (gift from J. Rich, University of California, San Diego) were grown using Dulbecco's modified Eagle's medium (DMEM)/F-12 (50:50), containing L-glutamine (Corning), N2 and B27 supplements (Invitrogen), human epidermal growth factor (Shenandoah Biotechnology), human fibroblast growth factor (Shenandoah

Biotechnology), human leukemia inhibitor factor (Shenandoah Biotechnology), GlutaMAX (Life Technologies), and 1% penicillin/streptomycin antibiotics (Life Technologies). NHAs (gift from R. Pieper, University of California, San Francisco), U87MG, and LN2308 glioma cells were grown in 1× DMEM with glucose (4.5 g/liter), L-glutamine, and sodium pyruvate (Corning) containing 10% fetal bovine serum (FBS; Life Technologies) and 1% penicillin/streptomycin antibiotics (Life Technologies).

Generation of cells modified for IDH3α KD, KO, and overexpression

The *IDH3α* cDNA was cloned into the CSII-CMV-MCS-IRES2-Venus vector using unique Nhe I and Age I restriction sites. For virus production, human embryonic kidney (HEK) 293T cells were plated in T75 flasks. At 70% confluency, cells were transfected with 20 μg of *IDH3α* or empty vector control construct, 10 μg of pMD2.G (envelope), and 15 μg of psPAX2 (HIV-Gag-Pol-Rev), using Lipofectamine 2000 (Thermo Fisher Scientific) according to the manufacturer's instructions. For virus concentration, the cell supernatant was spun at 114g for 5 min to pellet debris. The supernatant was filtered using a 45-μm low-protein binding filter (Millipore) and centrifuged at 120,000g for 2 hours at 4°C. The virus pellet was resuspended in DMEM, aliquoted, and stored at –80°C. Mission shRNA lentiviral particles (pLKO.1-puro-CMV-tGFP) targeted to *IDH3α* were purchased from Sigma-Aldrich (sequences: sh2, TGTCTC-TATCGAAGGCTATAA; sh5, TTAAGTGTCTACCTGGTAAAT), including control particles (SHC003V). Viruses to generate CRISPR-Cas9 KO clones were purchased from Sigma-Aldrich. The viral plasmid (CRISPR12V-1EA, Sigma-Aldrich) contained both the sgRNA and the Cas9 protein along with green fluorescent protein (GFP), puromycin, and ampicillin. The following sequences were used: sgRNA 318, CCITTTGAAGACCCCAATAGCAG; sgRNA 329, CCAATAGCAGCCGGTCACCCA; and control sgRNA, CGCGATAGCGGAATATAT-TNGG. For lentiviral infection, cells were trypsinized and seeded at 50% confluency. The next day, cells were washed with phosphate-buffered saline (PBS). Opti-MEM containing polybrene (0.8 μg/ml) was added or used for resuspension and dilution of virus (1:1000 or 3:1000 dilution of virus stocks). Cells were incubated at 37°C and 5% CO₂ for 4 to 6 hours, before adding fresh full growth medium. After 3 to 6 days, the cells were trypsinized, washed with PBS, and resuspended in PBS for flow cytometry-based cell sorting using the GFP signal. Sorted cells then underwent limited dilution cloning. Single-cell clones were grown up and screened for *IDH3α* KO via WB. Clones that showed lack of *IDH3α* expression were further subcloned.

Cell growth curves

Cells were seeded into six-well plates at 50,000 cells per well (day 0). Every 3 days, cells were trypsinized, stained with trypan blue for assessment of cell viability, and counted twice using an automated cell counter.

Transwell invasion assay

Fisher/Corning BioCoat invasion chamber 24 wells (catalog no. 8774122) were used for this assay, and the experiments outlined below were carried out according to the manufacturer's protocol. Briefly, plates/transwells were removed from –20°C and left at room temperature (RT) for 1 hour. Bicarbonate-containing medium was added to each transwell, and wells were incubated for 2 hours in a

humidified tissue culture incubator. After the medium was removed, a cell suspension of 500,000 cells/0.5 ml in medium without any growth supplements was added to each transwell, and 0.5 ml of full medium was placed in the bottom well. The plate was then incubated in a humidified tissue culture incubator for 22 to 24 hours. Subsequently, the nonmigratory cells were washed off with a cotton tip, and wells were fixed and stained with the Richard-Allan Scientific Three-Step Stain. The wells were then dried overnight before mounting on microscope slides for imaging.

Generating IDH3α deletion mutants

Mutagenesis primers were designed to delete the MTS sequence of the *IDH3α* gene: forward, ACTTTAATTCAGGAGATGGTATTGGCCCA; reverse, CATGCTAGCGGATCTGACGGTTCCTAAAC. These primers were then added at 0.5 μM concentration to 100 ng of *IDH3α* vector DNA along with 200 μM of deoxynucleotide triphosphate, 1.25 U of PrimeSTAR HS (catalog no. R010A, Takara), and PrimeSTAR 5× Buffer to obtain a 1× final concentration. Reaction mixtures were supplemented with nuclease-free water up to a volume of 50 μl. A polymerase chain reaction (PCR) was carried out on a thermocycler using the following parameters: 95°C for 2 min, then 30 cycles of 97°C for 10 s, 68°C for 1 min, 72°C for 10 min, and then 4°C to hold. Subsequently, 20 U of Dpn I (catalog no. R0176, New England Biolabs) was added directly to the PCR tube for 1 hour. The PCR was then run on a gel. The product band was excised, extracted, and treated with 10 U of T4 PNK (catalog no. M0201, New England Biolabs) in 1× of T4 PNK buffer (catalog no. B0201, New England Biolabs), 1 mM ATP (catalog no. P0756, New England Biolabs), and nuclease-free water (total volume, 50 μl). The samples were then incubated at 37°C for 30 min and heat-inactivated at 65°C for 20 min. One microliter of T4 DNA ligase (catalog no. M1804, Promega) was added to the reaction tube. After 3 hours of incubation at RT, the plasmids were then transformed into bacteria and the deletion of MTS was confirmed by sequencing.

Immunoprecipitation and mass spectrometry

Cells were lysed in IP buffer [50 mM tris-HCl (pH 7.5), 150 mM NaCl, 5 mM EDTA, 1% lauryl maltose neopentyl glycol (Anatrace), 1× protease inhibitor cocktail, and 1× phosphatase inhibitor]. Five micrograms of *IDH3α* antibody (ab58641, Abcam) or control rabbit IgG antibody (sc-2030, Santa Cruz Biotechnology) was added to 500 mg of cell lysate. The samples were then left to rotate at 4°C overnight. Dynabeads (50 μl per sample) (10004D, Life Technologies) were added. Upon placement on a magnet, beads were washed with IP buffer. To elute immunoprecipitated proteins, beads were resuspended in 2 × 30 μl of glycine buffer [100 mM glycine (pH 2.5), adjusted with HCl]. Peptides were analyzed by LC-MS/MS using the Dionex UltiMate 3000 Rapid Separation nanoLC coupled to a linear ion trap—Orbitrap hybrid mass spectrometer (LTQ Velos Orbitrap, Thermo Fisher Scientific, San Jose, CA, USA). Proteins were identified from the MS raw files using the Mascot search engine (Matrix Science). MS/MS spectra were searched against the Swiss-Prot human database. All searches included carbamidomethyl cysteine as a fixed modification and oxidized Met, deamidated Asn and Gln, and acetylated N terminus as variable modifications. Three missed tryptic cleavages were allowed. The MS¹ precursor mass tolerance was set to 20 parts per million, and the MS² tolerance was set to 0.6 Da. A 1% FDR cutoff was applied at the protein level.

Coimmunoprecipitation

Cells were grown in 10- or 15-cm dishes. At 80 to 90% confluency, plates were washed with cold PBS and collected in lysis buffer [50 mM Tris-HCl (pH 7.5), 150 mM NaCl, 5 mM EDTA, 1% lauryl maltose neopentyl glycol, 1× protease inhibitor cocktail, and 1× phosphatase inhibitor]. The cell lysis solution was vortexed every 5 min for 30 min while kept on ice. The samples were spun down at 4°C for 15 min at 16,100g. The supernatant was then collected, and protein concentration was determined by Bradford assay. Total protein (500 to 1000 µg) was used for IPs with IgG control and specific antibodies [i.e., anti-IDH3α antibody (5 µg; ab58641, Abcam) and anti-cSHMT antibody (5 µg; ab186130, Abcam)]. Total protein (5 to 20 µg) was used as input. Samples were incubated at 4°C overnight while rotating. Dynabeads (50 µl per sample) (10004D, Life Technologies) were added, and after 30-min incubation at RT, beads were washed with PBS + 1× protease inhibitor and resuspended in 25 µl of NuPAGE LDS sample buffer (Life Technologies) + 5% β-mercaptoethanol. The samples were then heated at 95°C for 10 min and analyzed via WB.

WB analysis

Samples were run on NuPAGE 4 to 12% bis-tris gels (Life Technologies) and transferred to Hybond P polyvinylidene difluoride membranes (Genesee Scientific, GE). Membranes were washed for 5 min in PBS + 0.05% Tween 20 (PBS-T), blocked with 5% milk in PBS-T for 1 hour, incubated with primary antibodies overnight, washed three times with PBS-T for 10 min per wash, and developed with secondary goat anti-rabbit, goat anti-mouse, or donkey anti-goat IgG antibodies (Santa Cruz Biotechnology) in 5% milk PBS-T. After three more washes for 10 min each with PBS-T, membranes were developed with SuperSignal enhanced chemiluminescence (ECL) (Thermo Fisher Scientific) following the manufacturer's protocol. The following primary antibodies were used: anti-cleaved caspase-3 (9664, Cell Signaling), anti-cleaved caspase-7 (9491, Cell Signaling), anti-IDH3α (SAB100035, Sigma-Aldrich), anti-Hsp70 (610607, BD Biosciences), anti-cSHMT (ab186130, Abcam), anti-H3 (4499S, Cell Signaling), and anti-COXIV (4850S, Cell Signaling).

NAD⁺/NADPH, SAM/SAH, HCY, αKG, IDH activity, 5mC and 5hmC, and NAD⁺/NADH quantification

The following kits were used according to the manufacturer's instructions: BioVision's colorimetric assay (catalog no. K347-100) for NADP⁺ and NADPH quantification; ELISA kits (Cell Biolabs) for SAM, SAH (catalog no. STA-671-C), and HCY (catalog no. STA-670) quantification; Abcam's colorimetric kit (catalog no. ab65348) for quantification of NAD⁺ and NADH levels; BioVision's colorimetric assay (catalog no. K677-100) for αKG quantification; BioVision's isocitrate dehydrogenase activity colorimetric assay (catalog no. K756-100) using NAD⁺ as cofactor for assessment of IDH3 activity; Epigentek's MethylFlash Methylated DNA 5mC Quantification Kit (Colorimetric; catalog no. P-1034-96); and Epigentek's MethylFlash Global DNA Hydroxymethylation (5hmC) ELISA Easy Kit (Colorimetric; catalog no. P-1032-96) measuring 5mC and 5hmC in extracted genomic DNA (gDNA). Final concentrations of formate, glycine, and αKG were 1 mM, 0.4 mM, and 5 µM, respectively.

ROS quantification

Cells were seeded at 500,000 cells per well into six-well plates, treated with 5 µM CellROX Deep Red reagent (C10422, Thermo Fisher Sci-

entific), and incubated for 30 min in a humidified tissue culture incubator. The medium was then removed, and cells were washed three times with PBS, followed by fixation with 3.7% formaldehyde for 15 min. Cells were then analyzed by flow cytometry.

DEVDase assay

Caspase-3/7 activation was measured by spectrophotometric detection using the BioVision Kit (catalog no. K106-25) according to the manufacturer's instructions.

Cell fractionation

Cells were collected by centrifugation at 1500g for 5 min. The pellet was resuspended in 200 µl of hypotonic buffer [10 mM Hepes (pH 8), 10 mM KCl, 1 mM EDTA, 1× protease inhibitor, 1.5 mM MgCl₂, 0.1 mM dithiothreitol (DTT), and 10 µM cytochalasin B] and incubated on ice for 30 min, followed by centrifugation for 5 min at 1500g. The supernatant was discarded, and the pellet was resuspended in 200 µl of hypotonic buffer. Next, the samples were homogenized with a 25-gauge needle and centrifuged at 400g for 10 min. The supernatant representing the cytosolic and mitochondrial fraction was retained. The pellet was washed with 500 µl of hypotonic buffer, followed by centrifugation at 400g for 10 min. The resulting pellet was washed twice with PBS (500 µl per wash) containing 1 mM EDTA, 1.5 mM MgCl₂, 0.1 mM DTT, and 10 µM cytochalasin B. The pellet was resuspended in 3 ml of S1 (0.25 mM sucrose, 10 mM MgCl₂ + 1× protease inhibitor). The S1/sample solution was layered over 3 ml of S2 (0.35 mM sucrose, 0.5 mM MgCl₂ + 1× protease inhibitor) by slowly pipetting S1 onto S2. Samples were centrifuged at 4°C for 10 min at 2178g. The supernatant was removed, and the pellet was resuspended in 3 ml of S2. The S2/sample solution was layered over a 3-ml layer of S3 (0.88 mM sucrose, 0.5 mM MgCl₂ + 1× protease inhibitor) by slowly pipetting S2 onto S3, and the final sample was centrifuged at 4°C for 10 min at 2178g. The supernatant was removed, and the pellet was resuspended in Thermo Fisher NER reagent + 1× protease inhibitor. The samples were vortexed for 15 s followed by an incubation period of 40 min on ice. Every 10 min, the samples were vortexed for 15 s. Samples were centrifuged at maximum speed (~16,000g) for 10 min. The resulting supernatant represented the nuclear fraction.

Cell cycle syncing

Cells were grown to 20 to 30% confluency, washed twice with 1× Dulbecco's PBS with calcium and magnesium (DPBS; 21-030-CV, Corning), and then treated with 2 mM thymidine in full medium for 18 hours. Cells were washed once with DPBS, resuspended in full medium for 9 hours, and treated again with 2 mM thymidine in full medium for 17 hours. Cells were stained with propidium iodide, and cell cycle distribution was analyzed by flow cytometry.

Tumor xenograft model

All animals used in the study were under an approved protocol of the Institutional Animal Care and Use Committee of Northwestern University. All cells were modified for luciferase expression, as described in our previous publication (5). GIC-387 expressing shIDH3α or shScr (2 × 10³ cells/2 µl), IDH3α KO and control WT NHAs (5 × 10⁴ cells/2 µl), NHA control and KO cultures stably expressing an IDH3α transgene or vector control, and GIC-20 overexpressing IDH3α and vector only (5 × 10⁴ cells/2 µl) were resuspended in Hank's balanced salt solution. Anesthetized 6- to 8-week-old female

CB17 SCID (severe combined immunodeficient) mice (Taconic Farms) were placed in stereotactic frames, and the surgical area was cleaned with betadine followed by 70% ethanol. Following a scalp incision, a 0.7-mm Burr hole was created in the skull with a microsurgical drill, 2-mm lateral right of the sagittal suture and 0.5-mm posterior to the bregma. Cells were injected through a Hamilton syringe after it was inserted 3 mm into the brain. Cells were injected at a rate of 1 μ l/min. Once surgery was completed, the skin was closed with sutures. Mice were euthanized at ethical end points based on observations of neurological impairment or severe changes in body weight. Eight to 10 animals were used in each group, and mice were randomized on the basis of body weight. The Kaplan-Meier method was used to plot survival, and significance was determined by the log-rank (Mantel-Cox) test.

In vivo bioluminescence imaging

Ten minutes after intravenous injection with 200 μ l of luciferin potassium salt (PerkinElmer) suspended in PBS, mice were anesthetized and imaged using the IVIS Spectrum (PerkinElmer). Bioluminescence was quantified using Living Imaging software (Caliper Life Sciences).

Immunohistochemistry

Tissue samples were collected with patient consent at the University of Kentucky and prepped as a TMA. Slides were heated at 60°C for 1 hour followed by deparaffinization and hydration, washed with water, placed into 1 \times Dako Target Retrieval Solution (S1699, Agilent), and subsequently incubated in the Biocare Medical Decloaking Chamber at 110°C for 10 min. Slides were washed twice with PBS for 3 min, 200 μ l of peroxidase block (Dako K4011, Agilent) was added, and slides were incubated for 10 min at RT followed by a PBS rinse. Next, two to five drops of protein block background with background sniper (BS966H, Biocare Medical) were added, and slides were incubated for 10 min at RT followed by 1 to 2 min of PBS rinse. IDH3 α antibody (HPA041465, Sigma-Aldrich) was added at a 1:400 dilution to the slides and incubated for 1 hour. Slides were then rinsed three times with tris-buffered saline/Tween 20 for 1 min each. Secondary antibody (Dako 4011, Agilent) was added and incubated for 35 min followed by three PBS washes. DAB (3,3'-diaminobenzidine) chromogen was added, incubated up to 3 min followed by counterstaining with hematoxylin, and then washed with water. The slides were then dehydrated, and coverslips were mounted with Permount. A licensed and practicing neuropathologist then scored the tissues as concerns IDH3 α staining intensity. For endothelial cell staining, tissue was deparaffinized followed by incubation with IDH3 α antibody (HPA041465, Sigma-Aldrich) overnight and then with CD31 antibody (sc-1506, Santa Cruz Biotechnology) for 1 hour. Samples were then blocked with 3% hydrogen peroxide in water for 10 min and with avidin/biotin for 15 min each. Blocking of nonspecific proteins was further achieved by incubating in 5% normal donkey serum for 30 min. The slides were then incubated with secondary Cy3 anti-rabbit for 1 hour and then secondary biotinylated anti-goat for 30 min, followed by treatment with the ABC Kit (PK-4000, Vector Labs) for 30 min. The slides were then incubated with a working solution of biotinyl tyramide for 5 min and then with Alexa Fluor 488-streptavidin for 30 min. Hoechst nuclear staining was performed for 10 min.

Metabolomics steady-state study

Cells (7.5×10^6 ; NHAs with CRISPR-mediated IDH3 α KO or NHAs overexpressing IDH3 α and their corresponding control cell lines) were

washed twice with DPBS and then snap frozen in liquid nitrogen. At Metabolon, samples were then processed by the automated Microlab STAR System (Hamilton). Recovery standards were added to all samples for quality control measures. Methanol was added to all samples. Each sample was shaken for 2 min followed by centrifugation to release metabolites. All samples had aliquots that underwent UPLC-MS/MS (Thermo Fisher Scientific) with reverse phase (RP) plus positive ion mode electrospray ionization (ESI), with RP plus negative ion mode ESI, or following hydrophilic interaction liquid chromatography column (Waters UPLC BEH Amide 2.1 mm \times 150 mm, 1.7 μ m) elution with negative ion mode ESI. Samples were reconstituted with solvents appropriate for each method and run alongside standards. Data were analyzed using Metabolon hardware and software. Compounds were identified on the basis of a narrow retention index that was then compared to a library of purified standards and MS/MS scores comparing the experimental spectrum to the library spectrum.

¹³C-labeled glucose tracer studies

Six-well plates were seeded with \sim 50,000 cells per well and allowed to attach overnight. The next day, all wells were washed with nutrient-free medium (DMEM; catalog no. A144300, Thermo Fisher Scientific) and then given medium supplemented with 4 mM glutamine (catalog no. G8540, Sigma-Aldrich), 10% dialyzed FBS (catalog no. A3382001, Thermo Fisher Scientific), 1 mM sodium pyruvate (catalog no. P5280, Sigma-Aldrich), and 25 mM uniformly ¹³C-labeled glucose (catalog no. 110187-42-3, Cambridge) for all time point samples excluding the 0-hour time point, which was labeled with 25 mM ¹²C-labeled glucose (catalog no. G7021, Sigma-Aldrich). At designated time points, the medium was removed, and the cells were washed with a cold 0.9% NaCl solution. Subsequently, 1 ml of ice-cold 80% methanol/water solution was added to each well, and the plate was placed at -80°C . After 15 min, the plates were removed from -80°C and placed on dry ice while the sample wells were scraped, and the cell/80% methanol solution was placed in collection tubes. The tubes were spun at 20,000g for 10 min at 4°C. The supernatant was taken and split between two tubes per sample. The amount of supernatant taken was based on cell counting to normalize the amount of cells per tube. Last, samples were dried in a speed vacuum at RT for 2 to 3 hours. This dry pellet was then stored at -80°C until analysis by LC-MS, as previously published (37).

¹³C-labeled serine tracer studies

Cells were seeded in six-well plates (1×10^6 per well) and allowed to attach (approximately 80% confluency). Cells were washed with PBS and given nutrient-free medium (MEM; catalog no. M0268, Sigma-Aldrich) supplemented with 10% dialyzed FBS (catalog no. A3382001, Thermo Fisher Scientific), 1 mM sodium pyruvate (catalog no. P5280, Sigma-Aldrich), penicillin/streptomycin, glycine (30 mg/liter), and labeled ¹³C₃ ¹⁵N₁ serine (catalog no. CNLM-474-H, Cambridge) for 3 hours. Cells were then washed with PBS and collected for DNA extraction, using the QIAamp DNA Mini Kit (catalog no. 51304, Qiagen), including ribonuclease treatment (catalog no. 1007885, Qiagen), following the manufacturer's instructions. DNA (2.5 μ g) was acid hydrolyzed at 40°C under nitrogen gas. Briefly, formic acid was added to the dry pellets and incubated at 130°C for 3.5 hours. The acid was dried at 40°C under nitrogen gas, and the pellets were resuspended in LC-MS-grade water. Cold solution of LC-MS-grade methanol (62.5%) and acetonitrile (37%) was added, and samples were dried in a speed vacuum at RT for 2 to 3 hours. This

dry pellet was then stored at -80°C until analysis by LC-MS, as previously published (38).

Seahorse assay

The day before the assay, the Seahorse cartridge was placed in the XF calibrant and incubated overnight at 37°C . On the day of the assay, cells were seeded into the Seahorse 96-well plate at 15,000 cells/80 μl per well. The plates were incubated at RT for 1 hour to allow even distribution of cells across the well floor. Before placing the sample plates in the Seahorse XF96 Analyzer, medium volume was adjusted to 175 μl in each well. Oligomycin at 2 μM , CCCP at 10 μM , and antimycin A and rotenone at 2 μM each, diluted in DMEM, were injected sequentially into each well including control wells, containing only medium, following the standard Seahorse protocol.

IF and confocal microscopy

Cells were seeded in either 10-cm dishes or 24-well plates containing synthetic poly-D-lysine/mouse laminin-coated 12-mm round coverslips (Corning) and allowed to attach. Cell medium was removed, and cells were washed with PBS before fixation with 4% paraformaldehyde in deionized water for 5 min. The coverslips were washed with PBS, and cells were permeabilized with PBS/0.2% Triton X-100 (EMD) for 5 min. The coverslips were washed with PBS, followed by PBS/1% FBS, and then blocked for 30 min in PBS/1% FBS. The blocking solution was removed, and primary antibodies diluted in PBS/1% FBS [i.e., anti-IDH3 α (5 $\mu\text{g}/\text{ml}$; ab58641, Abcam), anti-cSHMT (1:50; sc-514410, Santa Cruz Biotechnology), anti-lamin A (1:500; sc-6214, Santa Cruz Biotechnology), and anti-cytochrome c (1:500; 556432, BD Biosciences), together with Hoechst 33342 (1:10,000; Invitrogen)] were added and incubated with cells overnight at 4°C . Coverslips were washed twice with PBS/1% FBS, and the secondary antibody was added [Alexa Fluor 488 anti-goat or anti-rabbit, Alexa Fluor 648 anti-rabbit, or Alexa Fluor 568 anti-mouse (1:300; Invitrogen/Life Technologies)] for 1 hour at RT in the dark. The coverslips were washed once with PBS/1% FBS, twice with PBS, and once with water before being mounted on microscope slides. Slides were imaged using a Nikon A1R spectral microscope with a light-emitting diode power source. To quantify IDH3 α and cSHMT colocalization using ImageJ, a macro was designed that created a mask for cSHMT intracellular distribution, based on the Alexa Fluor 568 staining; appropriate thresholds were used to decrease background signal. The percentage of IDH3 α staining (Alexa Fluor 488) covered by the cSHMT mask was quantified relative to total IDH3 α staining, and thus, colocalizing with cSHMT was determined.

Reverse transcription quantitative PCR

mRNA expression was measured using SYBR green technology (Integrated DNA Technologies) and quantified using the $\Delta\Delta\text{C}_t$ method.

DNA global methylation array

DNA global methylation was measured in four biological replicates. Methylation levels were measured using the Infinium Human MethylationEPIC BeadChip Array (Illumina Inc., CA, USA), which targets more than 850,000 methylation sites. Samples were randomly plated on each chip. A 500-ng DNA sample was used to perform bisulfite conversion followed by methylation profiling according to Illumina's protocol. BeadChips were scanned with an Illumina iScan and analyzed using the Illumina GenomeStudio software. All experiments were conducted following the manufacturer's protocols.

RNA sequencing

RNA was extracted from control or IDH3 α KO NHAs using the RNeasy Kit (Qiagen) according to the manufacturer's protocol. RNA quality control was performed using an Agilent Bioanalyzer. RNA-seq libraries were generated using Illumina TruSeq mRNA stranded kits following Illumina protocols. Libraries were quantitated using an Agilent bioanalyzer, and the pooled libraries were sequenced with an Illumina HiSeq 4000 system using Illumina reagents and protocols.

Preprocessing of RNA-seq expression data

RNA-seq data were preprocessed using RSEM software package with in-built STAR alignment tool (39, 40). Raw sequence reads were aligned to human reference genome (GRCh37/hg19 assembly).

Differential expression analysis using DESeq2

Abundance quantifications were imported into R software, and gene expression matrix was constructed using R Bioconductor package tximport (41). Count values summarized by tximport were analyzed using the DESeq2 algorithm. Differential expression was defined at a threshold of FDR = 0.05 and absolute log fold change > 1.

Preprocessing of methylation microarray data

Methylation microarray data from Illumina Infinium Human MethylationEPIC BeadChip platform were analyzed using R Bioconductor package minfi (42). Raw IDAT files were loaded into R software, and raw intensity signals were preprocessed and normalized using functional normalization algorithm optimized for multicondition studies (43). The resulting normalized β values were further converted to M values [$M = \log_2(\beta/(1 - \beta))$] for downstream statistical analyses. Quality control was performed by manually checking quality control density plots. Probes with single-nucleotide polymorphisms were dropped as they are prone to affect methylation measurements. All probes were annotated using human reference genome GRCh37/hg19 assembly. Quality as well as sample-wise pattern of the preprocessed data were preliminarily visualized by principal components analysis.

Differentially methylated position analysis using Limma

To identify which individual CpG loci were differentially methylated between IDH3 α KO and control conditions, we performed differentially methylated positions (DMP) analysis using Limma algorithm (44). The M -value matrix was subjected to lmfitt to compute the mean difference between conditions. Differentially methylated CpG loci was defined as Benjamini-Hochberg adjusted $P < 0.05$ and absolute M -value difference greater than 1 ($|\Delta M\text{-value}| > 1$).

Differentially methylated region analysis using DMRcate

To identify and visualize consistent methylation patterns within continuous genomic regions (e.g., CpG islands), we also performed differentially methylated regions (DMR) analysis using DMRcate package, which applies a Gaussian kernel smoothing to demarcate adjacent CpG sites within a genomic window (45). We applied the kernel bandwidth $\lambda = 1000$ and scaling factor $C = 2$ following the recommended setting. We visualized the most significant DMRs in terms of minimum FDR using the DMR.plot function within the package.

Integrative analysis of expression and methylation data

To elucidate the relationship between expression level of a gene and methylation level of a CpG locus within that gene, we performed an

integrative analysis combining our RNA-seq expression and methylation array data. To associate a methylation probe with a gene, we defined the putative promoter region as -2 kb to $+500$ base pairs (bp) of the transcription start site (TSS) and linked all CpG loci with the corresponding gene. Genes with low expression were removed. We used trimmed mean of M values (TMM) normalization across samples to adjust the difference in library size and \log_2 transformed the normalized expression values (46). We identified 209,063 CpG-gene pairs between 23,967 genes and 835,778 CpG sites. We then performed Pearson correlation analysis between gene expression and methylation data to identify statistically significant CpG-gene pairs. A positive correlation indicates methylation and expression change in the same direction, while a negative correlation implies changes in the opposite direction.

5mC/5hmC DNA dot blot

gDNA extracted in water was diluted to a final concentration of 400 ng/ μ l in 10- μ l volume for both NHA control and IDH3 α KO. Subsequently, to each dilution, 200 μ l of 6 \times saline sodium citrate (SSC) was added. Each sample was heated at 100°C for 10 min and allowed to cool on ice, and 200 μ l of ice-cold 20 \times SSC was added. Meanwhile, nitrocellulose membrane and two filter papers were wetted with 6 \times SSC and then mounted on a 96-well dot blot apparatus. To the wells to be used, 500 μ l of water was added and pulled through the membrane with gentle vacuum pressure. Subsequently, the diluted samples were added and pulled through. Last, the membrane was washed with 500 μ l of 2 \times SSC solution and pulled through the membrane. The membrane was allowed to air dry before ultraviolet DNA cross-linking for 5 min at 100 μ J/cm². The membrane was incubated in 5% milk overnight. The following day, 5mC or 5hmC antibodies (#MABE146, Millipore and #39769, Active Motif) were added to the membrane (1:1000 dilution in 5% milk) for 1 hour, washed three times with PBS-T (5 min each), incubated with secondary mouse antibody (1:2500) for 30 min, washed three times with PBS-T again, and then developed with ECL. The loading was determined by 0.02% methylene blue stain.

MTT assay

Cells were seeded at 10,000 cells per well in a 96-well plate and treated with vehicle/Opti-MEM, or 0.1, 1, 10, or 100 μ M MTX, 0.5 mM NAC, or 1 mM formate/0.4 mM glycine. The MTT assay was performed following the manufacturer's protocol (American Type Culture Collection).

Histone methylation

NHA controls and NHA IDH3 α KO cells were grown in 10-cm dishes. At confluency, 1 million cells were collected for every biological replicate, three per group, washed with PBS, and flash frozen in liquid nitrogen. The samples were analyzed on the TSQ Quantum Ultra MS. To prepare the samples for MS, histones were acid extracted, washed, and then subjected to propionylation and tryptic digestion (47). Samples were then resuspended in 50 μ l of 0.1% trifluoroacetic acid/mH₂O. For each sample, we prepared three technical replicates. We used 3 μ l per injection. HeLa cells were used as quality control and for data comparison. Targeted analysis of unmodified and various modified histone peptides was performed.

Statistical analysis

All graphical and WB data are a culmination or representation of $n \geq 3$ biological replicates with technical replicates ($n \geq 3$) within

each biological replicate. Data are represented as means \pm SD (or SEM) for bioluminescence. Two-tailed Student's t test was used to compare control to experimental groups, unless otherwise stated. $P \leq 0.05$ was considered to be statistically significant.

SUPPLEMENTARY MATERIALS

Supplementary material for this article is available at <http://advances.sciencemag.org/cgi/content/full/5/1/eaat0456/DC1>

Fig. S1. IDH3 α is confined to the nuclear periphery and highly expressed in the tumor-associated vasculature.

Fig. S2. IDH3 α regulates cellular invasiveness.

Fig. S3. Subcellular redistribution of IDH3 α and colocalization with cSHMT.

Fig. S4. Effect of IDH3 α ablation on glycolysis, TCA, and folate one-carbon metabolism.

Fig. S5. IDH3 α KO does not affect global histone methylation status but affects DNA methylation.

Fig. S6. IDH3 α loss of function through impact on DNA methylation regulates gene expression.

Fig. S7. IDH3 α expression affects MTX treatment response.

Table S1. Alterations in IDH3 α expression lead to widespread metabolomic changes.

REFERENCES AND NOTES

1. K. Dalziel, Isocitrate dehydrogenase and related oxidative decarboxylases. *FEBS Lett.* **117**, K45–K55 (1980).
2. L. Dang, D. W. White, S. Gross, B. D. Bennett, M. A. Bittinger, E. M. Driggers, V. R. Fantin, H. G. Jang, S. Jin, M. C. Keenan, K. M. Marks, R. M. Prins, P. S. Ward, K. E. Yen, L. M. Liau, J. D. Rabinowitz, L. C. Cantley, C. B. Thompson, M. G. Vander Heiden, S. M. Su, Cancer-associated IDH1 mutations produce 2-hydroxyglutarate. *Nature* **462**, 739–744 (2009).
3. M. E. Figueroa, O. Abdel-Wahab, C. Lu, P. S. Ward, J. Patel, A. Shih, Y. Li, N. Bhagwat, A. Vasanthakumar, H. F. Fernandez, M. S. Tallman, Z. Sun, K. Wolniak, J. K. Peeters, W. Liu, S. E. Choe, V. R. Fantin, E. Paietta, B. Löwenberg, J. D. Licht, L. A. Godley, R. Delwel, P. J. Valk, C. B. Thompson, R. L. Levine, A. Melnick, Leukemic IDH1 and IDH2 mutations result in a hypermethylation phenotype, disrupt TET2 function, and impair hematopoietic differentiation. *Cancer Cell* **18**, 553–567 (2010).
4. D. R. Wahl, J. Dresser, K. Wilder-Romans, J. D. Parsels, S. G. Zhao, M. Davis, L. Zhao, M. Kachman, S. Wernisch, C. F. Burant, M. A. Morgan, F. Y. Feng, C. Speers, C. A. Lyssiotis, T. S. Lawrence, Glioblastoma therapy can be augmented by targeting IDH1-mediated NADPH biosynthesis. *Cancer Res.* **77**, 960–970 (2017).
5. A. E. Calvert, A. Chalastanis, Y. Wu, L. A. Hurley, F. M. Kouri, Y. Bi, M. Kachman, J. L. May, E. Bartom, Y. Hua, R. K. Mishra, G. E. Schiltz, O. Dubrovskiy, A. P. Mazar, M. E. Peter, H. Zheng, C. D. James, C. F. Burant, N. S. Chandel, R. V. Davuluri, C. Horbinski, A. H. Stegh, Cancer-associated IDH1 promotes growth and resistance to targeted therapies in the absence of mutation. *Cell Rep.* **19**, 1858–1873 (2017).
6. J. L. Gabriel, P. R. Zervos, G. W. E. Plaut, Activity of purified NAD-specific isocitrate dehydrogenase at modulator and substrate concentrations approximating conditions in mitochondria. *Metabolism* **35**, 661–667 (1986).
7. F. Qi, X. Chen, D. A. Beard, Detailed kinetics and regulation of mammalian NAD-linked isocitrate dehydrogenase. *Biochim. Biophys. Acta* **1784**, 1641–1651 (2008).
8. K. P. Bzymek, R. F. Colman, Role of α -Asp¹⁸¹, β -Asp¹⁹², and γ -Asp¹⁹⁰ in the distinctive subunits of human NAD-specific isocitrate dehydrogenase. *Biochemistry* **46**, 5391–5397 (2007).
9. S. Soundar, M. O'Hagan, K. S. Fomulu, R. F. Colman, Identification of Mn²⁺-binding aspartates from α , β , and γ subunits of human NAD-dependent isocitrate dehydrogenase. *J. Biol. Chem.* **281**, 21073–21081 (2006).
10. D. Zhang, Y. Wang, Z. Shi, J. Liu, P. Sun, X. Hou, J. Zhang, S. Zhao, B. P. Zhou, J. Mi, Metabolic reprogramming of cancer-associated fibroblasts by IDH3 α downregulation. *Cell Rep.* **10**, 1335–1348 (2015).
11. L. Zeng, A. Morinibu, M. Kobayashi, Y. Zhu, X. Wang, Y. Goto, C. J. Yeom, T. Zhao, K. Hirota, K. Shinomiya, S. Itasaka, M. Yoshimura, G. Guo, E. M. Hammond, M. Hiraoka, H. Harada, Aberrant IDH3 α expression promotes malignant tumor growth by inducing HIF-1-mediated metabolic reprogramming and angiogenesis. *Oncogene* **34**, 4758–4766 (2014).
12. D. Krell, M. Assoku, M. Galloway, P. Mulholland, I. Tomlinson, C. Bardella, Screen for IDH1, IDH2, IDH3, D2HGDH and L2HGDH mutations in glioblastoma. *PLOS ONE* **6**, e19868 (2011).
13. R. B. Puchalski, N. Shah, J. Miller, R. Dalley, S. R. Nomura, J.-G. Yoon, K. A. Smith, M. Lankerovich, D. Bertagnoli, K. Bickley, A. F. Boe, K. Brouner, S. Butler, S. Caldejon, M. Chapin, S. Datta, N. Dee, T. Desta, T. Dolbear, N. Dotson, A. Ebbert, D. Feng, X. Feng, M. Fisher, G. Gee, J. Goldy, L. Gourley, B. W. Gregor, G. Gu, N. Hejazinia, J. Hohmann, P. Hothi, R. Howard, K. Joines, A. Kriedberg, L. Kuan, C. Lau, F. Lee, H. Lee, T. Lemon, F. Long, N. Mastan, E. Mott, C. Murthy, K. Ngo, E. Olson, M. Reding, Z. Riley, D. Rosen, D. Sandman, N. Shapovalova, C. R. Slaughterbeck, A. Sodd, G. Stockdale, A. Szafer, W. Wakeman, P. E. Wahnoutka, S. J. White, D. Marsh, R. C. Rostomily, L. Ng, C. Dang,

- A. Jones, B. Keogh, H. R. Gittleman, J. S. Barnholtz-Sloan, P. J. Cimino, M. S. Uppin, C. D. Keene, F. R. Farrokhi, J. D. Lathia, M. E. Berens, A. Iavarone, A. Bernard, E. Lein, J. W. Phillips, S. W. Rostad, C. Cobbs, M. J. Hawrylycz, G. D. Foltz, An anatomic transcriptional atlas of human glioblastoma. *Science* **360**, 660–663 (2018).
14. The Cancer Genome Atlas Research Network, Comprehensive genomic characterization defines human glioblastoma genes and core pathways. *Nature* **455**, 1061–1068 (2008).
15. P. F. Cohen, R. F. Colman, Diphosphopyridine nucleotide dependent isocitrate dehydrogenase from pig heart. Characterization of active substrate and modes of regulation. *Biochemistry* **11**, 1501–1508 (1972).
16. A. T. Qattan, M. Radulovic, M. Crawford, J. Godovac-Zimmermann, Spatial distribution of cellular function: The partitioning of proteins between mitochondria and the nucleus in MCF7 breast cancer cells. *J. Proteome Res.* **11**, 6080–6101 (2012).
17. R. Nagaraj, M. S. Sharpley, F. Chi, D. Braas, Y. Zhou, R. Kim, A. T. Clark, U. Banerjee, Nuclear localization of mitochondrial TCA cycle enzymes as a critical step in mammalian zygotic genome activation. *Cell* **168**, 210–223.e11 (2017).
18. D. D. Anderson, C. F. Woeller, E.-P. Chiang, B. Shane, P. J. Stover, Serine hydroxymethyltransferase anchors de novo thymidylate synthesis pathway to nuclear lamina for DNA synthesis. *J. Biol. Chem.* **287**, 7051–7062 (2012).
19. C. F. Woeller, D. D. Anderson, D. M. E. Szebenyi, P. J. Stover, Evidence for small ubiquitin-like modifier-dependent nuclear import of the thymidylate biosynthesis pathway. *J. Biol. Chem.* **282**, 17623–17631 (2007).
20. G. S. Ducker, J. D. Rabinowitz, One-carbon metabolism in health and disease. *Cell Metab.* **25**, 27–42 (2017).
21. N. I. Krupenko, M. E. Dubard, K. C. Strickland, K. M. Moxley, N. V. Oleinik, S. A. Krupenko, ALDH1L2 is the mitochondrial homolog of 10-formyltetrahydrofolate dehydrogenase. *J. Biol. Chem.* **285**, 23056–23063 (2010).
22. A. J. MacFarlane, D. D. Anderson, P. Flodby, C. A. Perry, R. H. Allen, S. P. Stabler, P. J. Stover, Nuclear localization of de novo thymidylate biosynthesis pathway is required to prevent uracil accumulation in DNA. *J. Biol. Chem.* **286**, 44015–44022 (2011).
23. A. J. MacFarlane, X. Liu, C. A. Perry, P. Flodby, R. H. Allen, S. P. Stabler, P. J. Stover, Cytoplasmic serine hydroxymethyltransferase regulates the metabolic partitioning of methylenetetrahydrofolate but is not essential in mice. *J. Biol. Chem.* **283**, 25846–25853 (2008).
24. S. Pollari, S.-M. Käkönen, H. Edgren, M. Wolf, P. Kohonen, H. Sara, T. Guise, M. Nees, O. Kallioniemi, Enhanced serine production by bone metastatic breast cancer cells stimulates osteoclastogenesis. *Breast Cancer Res. Treat.* **125**, 421–430 (2011).
25. F. Kottakis, B. N. Nicolay, A. Roumane, R. Karnik, H. Gu, J. M. Nagle, M. Boukhali, M. C. Hayward, Y. Y. Li, T. Chen, M. Liesa, P. S. Hammerman, K. K. Wong, D. N. Hayes, O. S. Shrihail, N. J. Dyson, W. Haas, A. Meissner, N. Bardeesy, LKB1 loss links serine metabolism to DNA methylation and tumorigenesis. *Nature* **539**, 390–395 (2016).
26. T. Laukka, C. J. Mariani, T. Ihanntola, J. Z. Cao, J. Hokkanen, W. G. Kaelin Jr., L. A. Godley, P. Koivunen, Fumarate and succinate regulate expression of hypoxia-inducible genes via TET enzymes. *J. Biol. Chem.* **291**, 4256–4265 (2016).
27. C. A. Lewis, S. J. Parker, B. P. Fiske, D. McCloskey, D. Y. Gui, C. R. Green, N. I. Vokes, A. M. Feist, M. G. Vander Heiden, C. M. Metallo, Tracing compartmentalized NADPH metabolism in the cytosol and mitochondria of mammalian cells. *Mol. Cell* **55**, 253–263 (2014).
28. C. R. Gault, L. M. Obeid, Y. A. Hannun, An overview of sphingolipid metabolism: From synthesis to breakdown. *Adv. Exp. Med. Biol.* **688**, 1–23 (2010).
29. M. J. Osborn, M. Freeman, F. M. Huennekens, Inhibition of dihydrofolate reductase by aminopterin and amethopterin. *Proc. Soc. Exp. Biol. Med.* **97**, 429–431 (1958).
30. E. Chu, J. C. Drake, D. Boarman, J. Baram, C. J. Allegra, Mechanism of thymidylate synthase inhibition by methotrexate in human neoplastic cell lines and normal human myeloid progenitor cells. *J. Biol. Chem.* **265**, 8470–8478 (1990).
31. D. C. Phillips, K. J. Woollard, H. R. Griffiths, The anti-inflammatory actions of methotrexate are critically dependent upon the production of reactive oxygen species. *Br. J. Pharmacol.* **138**, 501–511 (2003).
32. A. E. Beaudin, E. V. Abarinov, D. M. Noden, C. A. Perry, S. Chu, S. P. Stabler, R. H. Allen, P. J. Stover, *Shmt1* and de novo thymidylate biosynthesis underlie folate-responsive neural tube defects in mice. *Am. J. Clin. Nutr.* **93**, 789–798 (2011).
33. A. Paone, M. Marani, A. Fiascarelli, S. Rinaldo, G. Giardina, R. Contestabile, A. Paiardini, F. Cutruzzola, SHMT1 knockdown induces apoptosis in lung cancer cells by causing uracil misincorporation. *Cell Death Dis.* **5**, e1525 (2014).
34. O. D. K. Maddocks, C. F. Labuschagne, P. D. Adams, K. H. Vousden, Serine metabolism supports the methionine cycle and DNA/RNA methylation through de novo ATP synthesis in cancer cells. *Mol. Cell* **61**, 210–221 (2016).
35. C. Lu, C. B. Thompson, Metabolic regulation of epigenetics. *Cell Metab.* **16**, 9–17 (2012).
36. M. Mehrmohamadi, X. Liu, A. A. Shestov, J. W. Locasale, Characterization of the usage of the serine metabolic network in human cancer. *Cell Rep.* **9**, 1507–1519 (2014).
37. M. V. Liberti, Z. Dai, S. E. Wardell, J. A. Baccile, X. Liu, X. Gao, R. Baldi, M. Mehrmohamadi, M. O. Johnson, N. S. Madhukar, A. A. Shestov, I. I. C. Chio, O. Elemento, J. C. Rathmell, F. C. Schroeder, D. P. McDonnell, J. W. Locasale, A predictive model for selective targeting of the Warburg effect through GAPDH inhibition with a natural product. *Cell Metab.* **26**, 648–659.e8 (2017).
38. American Diabetes Association, J. P. Bantle, J. Wylie-Rosett, A. L. Albright, C. M. Apovian, N. G. Clark, M. J. Franz, B. J. Hoogwerf, A. H. Lichtenstein, E. Mayer-Davis, A. D. Mooradian, M. L. Wheeler, Nutrition recommendations and interventions for diabetes: A position statement of the American Diabetes Association. *Diabetes Care* **31** (suppl. 1), S61–S78 (2008).
39. B. Li, C. N. Dewey, RSEM: Accurate transcript quantification from RNA-seq data with or without a reference genome. *BMC Bioinf.* **12**, 323 (2011).
40. A. Dobin, C. A. Davis, F. Schlesinger, J. Drenkow, C. Zaleski, S. Jha, P. Batut, M. Chaisson, T. R. Gingeras, STAR: Ultrafast universal RNA-seq aligner. *Bioinformatics* **29**, 15–21 (2013).
41. C. Soneson, M. I. Love, M. D. Robinson, Differential analyses for RNA-seq: Transcript-level estimates improve gene-level inferences. *F1000Res.* **4**, 1521 (2015).
42. M. J. Aryee, A. E. Jaffe, H. Corrada-Bravo, C. Ladd-Acosta, A. P. Feinberg, K. D. Hansen, R. A. Izarary, Minfi: A flexible and comprehensive Bioconductor package for the analysis of Infinium DNA methylation microarrays. *Bioinformatics* **30**, 1363–1369 (2014).
43. J.-P. Fortin, A. Labbe, M. Lemire, B. W. Zanke, T. J. Hudson, E. J. Fertig, C. M. T. Greenwood, K. D. Hansen, Functional normalization of 450k methylation array data improves replication in large cancer studies. *Genome Biol.* **15**, 503 (2014).
44. M. E. Ritchie, B. Phipson, D. Wu, Y. Hu, C. W. Law, W. Shi, G. K. Smyth, *limma* powers differential expression analyses for RNA-sequencing and microarray studies. *Nucleic Acids Res.* **43**, e47 (2015).
45. T. J. Peters, M. J. Buckley, A. L. Statham, R. Pidsley, K. Samaras, R. V. Lord, S. J. Clark, P. L. Molloy, De novo identification of differentially methylated regions in the human genome. *Epigenet. Chromatin* **8**, 6 (2015).
46. M. D. Robinson, A. Oshlack, A scaling normalization method for differential expression analysis of RNA-seq data. *Genome Biol.* **11**, R25 (2010).
47. B. A. Garcia, S. Mollah, B. M. Ueberheide, S. A. Busby, T. L. Muratore, J. Shabanowitz, D. F. Hunt, Chemical derivatization of histones for facilitated analysis by mass spectrometry. *Nat. Protoc.* **2**, 933–938 (2007).

Acknowledgments: We would like to acknowledge support provided by the following cores at the Northwestern University Feinberg School of Medicine and the Robert H. Lurie Comprehensive Cancer Center (RHLCC): Center for Advanced Microscopy/Nikon Imaging Center, NUSeq, Nervous System Tumor Bank, RHLCC—Flow Cytometry Core, RHLCC Metabolomics Core, and the Mouse Histology and Phenotyping Laboratory. Proteomics services were performed by the Northwestern Proteomics Core Facility, supported by NCI CCSG (P30 CA060553) and National Resource for Translational and Developmental Proteomics (P41 GM1108569). RNA-seq was performed by the University of Chicago Genomics Facility. **Funding:** This research was supported by the Center for Cancer Nanotechnology Excellence Initiative of the NIH under award nos. U54 CA151880 and 199091, R01CA208783, and a brain tumor SPORE grant (P50CA221747), all to A.H.S. J.L.M. was supported in part by NIH/SCI training grants T32 CA09560 and T32 GM008152. Support from R01CA193256 and P30CA014236 to J.W.L. and from R01LM011297 to R.V.D. is acknowledged. N.S.C. is supported by R35CA197532 and is a SAB member of Rafael Pharmaceuticals. **Author contributions:** J.L.M., F.M.K., and A.H.S. designed the experiments. F.M.K. and A.H.S. supervised the study. J.L., P.G., A.L., J.W.L., and N.S.C. designed and performed the metabolite tracing experiments and edited the manuscript. J.L.M. conducted the experiments and analyzed the data for all in vitro studies. L.A.H. and S.T.-G. performed all animal experiments, monitored the mice for survival, and extracted tumor-bearing brains. Y.J. and R.V.D. conducted the DNA methylation and RNA-seq analysis. A.E.C. conducted the NADPH/NADP⁺ studies. C.M.H. scored and analyzed the tissue stainings for patient-derived and xenografted tumors. **Competing interests:** The authors declare that they have no competing interests. **Data and materials availability:** All data needed to evaluate the conclusions in the paper are present in the paper and/or the Supplementary Materials. For the RNA-seq and methylation array data, they can be found at the Gene Expression Omnibus database under accession numbers GSE115364 and GSE115382, respectively. Additional data related to this paper may be requested from the authors.

Submitted 18 January 2018
Accepted 26 November 2018
Published 2 January 2019
10.1126/sciadv.aat0456

Citation: J. L. May, F. M. Kouri, L. A. Hurley, J. Liu, S. Tommasini-Ghelfi, Y. Ji, P. Gao, A. E. Calvert, A. Lee, N. S. Chandel, R. V. Davuluri, C. M. Horbinski, J. W. Locasale, A. H. Stegh, IDH3 α regulates one-carbon metabolism in glioblastoma. *Sci. Adv.* **5**, eaat0456 (2019).